

STABILITY OF NANOPOROUS METALS

Douglas Crowson

Dissertation submitted to the Faculty of the Virginia Polytechnic Institute and State University in partial fulfillment of the requirements for the degree of

Doctor of Philosophy
in
Materials Science and Engineering

Sean Gerald Corcoran, Chair
Diana Farkas, Co-Chair
William T. Reynolds Jr.
Yu Wang
Romesh Batra

June 14, 2006
Blacksburg, Virginia

Keywords: dealloying, porous metals, EAM, surface relaxation, surface stress

Copyright 2006, Douglas A. Crowson

STABILITY OF NANOPOROUS METALS

Douglas A. Crowson

ABSTRACT

A study of the stability of bicontinuous nanoporous metals is presented. Atomic scale simulations are used to probe the dominant mechanisms of geometric relaxation in these materials. A method is presented for generating model bicontinuous metal / void structures for use in atomistic simulations of bicontinuous nanoporous solids. The structures are generated with periodic boundary conditions using a phase-field model to simulate the spinodal decomposition of an ideal system. One phase in the model is then associated with the pore volume while the other phase is associated with the metal ligaments. Small angle neutron scattering was used to quantitatively compare experimental samples to those generated by the phase field method.

EAM results using model structures with experimentally accessible length scales are presented which demonstrate the potential of such simulations in understanding the behavior of nanoporous metals. Simulated relaxations of these structures, as well as the relaxation of model spherical clusters, indicate that the surface relaxation effect dominates the overall dimensional relaxation of np-metals post processing. Capillary effects play a secondary role in the overall relaxation. The simulation results presented also identify a maximum surface area to volume ratio necessary to maintain mechanical stability beyond which the pore structure collapses.

Funding for this work was provided by the National Science Foundation under contract DMR-0301007

ACKNOWLEDGEMENTS

I would like to thank my Advisor Sean Corcoran for all of his support over the years that I have known him. I have thoroughly enjoyed the discussions we have had about science as well as other topics. This is something that I will surely miss.

I would also like to thank my Co-Advisor Diana Farkas for her guidance and encouragement during my time at Virginia Tech.

A special thank you goes to Alfredo Caro for providing with the opportunity to work at the Lawrence Livermore National Laboratory. I greatly appreciate the time I spent there with him and I learned quite a lot.

I would also like to say thank you to all of my committee members.

A special thank you goes out to the friends that I have made at Virginia Tech. They have helped to make my time here very interesting and enjoyable.

Most importantly I would like to say thank you to all of my family who have supported me through this process.

TABLE OF CONTENTS

CHAPTER 1 INTRODUCTION.....	1
CHAPTER 2 BACKGROUND AND LITERATURE REVIEW	5
2.1 DEALLOYING	5
2.2 SURFACE STRESS AND ELECTROCAPILLARITY	8
2.3 MECHANICAL FAILURE OF POROUS MATERIALS.....	13
2.4 CLASSICAL ATOMISTIC SIMULATIONS	14
2.4.1 <i>Molecular Statics (MS)</i>	14
2.4.2 <i>Molecular Dynamics (MD)</i>	15
2.4.3 <i>Embedded Atom Method (EAM)</i>	20
CHAPTER 3 ATOMISTIC SIMULATIONS METHODS	22
3.1 EAM POTENTIALS FOR AU	22
3.1.1 <i>Johnson and Trimble Potentials</i>	22
3.1.2 <i>Hafel and Rosen Potentials</i>	27
3.2 EAM FOR ALLOYS.....	29
3.2.1 <i>Ta-W</i>	30
3.2.2 <i>Fe-Cr</i>	33
CHAPTER 4 SURFACE STRESS INDUCED STRAINS IN NANOPOROUS AU	36
4.1 GEOMETRIC RELAXATION OF NANOPOROUS METALS: ROLE OF SURFACE RELAXATION.....	36
4.2 SUPPLEMENTAL MATERIAL.....	51
4.2.1 <i>Bi-continuous Structures</i>	51
4.2.2 <i>Spherical Voids</i>	52
4.2.3 <i>Sphere Radius Definition</i>	54
4.2.4 <i>Directional Surface Relaxations</i>	55
4.2.5 <i>Mean Pressure in Ligaments</i>	59
CHAPTER 5 CAPILLARY DRIVEN MECHANICAL INSTABILITY OF NANOPOROUS METALS: BRIDGING LENGTH SCALES BETWEEN EXPERIMENT AND ATOMISTIC SIMULATION	62
5.1 CAPILLARY DRIVEN MECHANICAL INSTABILITY OF NANOPOROUS METALS: BRIDGING LENGTH SCALES BETWEEN EXPERIMENT AND ATOMISTIC SIMULATION	62
5.1.1 <i>Abstract</i>	62
5.1.2 <i>Letter</i>	63
5.1.3 <i>Methods</i>	77
5.1.4 <i>Acknowledgements</i>	78
5.1.5 <i>Supplemental Material</i>	79
CHAPTER 6 CONCLUSIONS	84
APPENDIX A	85
BIBLIOGRAPHY	99

LIST OF FIGURES

Figure 1-1 – Scanning electron micrograph of a nanoporous platinum formed by dealloying. Cu ₈₀ Pt ₂₀ in 1 M HClO ₄ at 1.24 V NHE for 20 hours followed by heat treatment at 800 C for 15 minutes (reprinted from Pugh, et al Journal of the Electrochemical Society 152, B455, 2005)[3].	2
Figure 2-1 -- Charge density ρ in semi-infinite crystals adjacent to an insulating interface (thickness d , relative dielectric constant ϵ) upon applying a voltage U , δ : screening length[29].	9
Figure 3-1 – Electron density function $f(r)$ for the Johnson and Trimble potentials in the effective pair format.	25
Figure 3-2 Embedding functions $F(\rho)$ for the Johnson and Trimble potentials in the effective pair format.	26
Figure 3-3 – Pair potential functions $V(r)$ for the Johnson and Trimble potentials in the effective pair format.	27
Figure 3-4 --Bulk Modulus (eV/Å ³) vs. Concentration (Ta) Blue dots are the	32
Figure 3-5 --Redlich-Kister fit to ab initio prediction of mixing energy for Fe-Cr.	33
Figure 3-6 -- The function $h(x)$ determined from fitting	34
Figure 3-7 -- Lattice parameter, bulk modulus and formation.	35
Figure 4-1 – Plot of strain vs. $(1/r)$, where r is the initial unrelaxed radius, observed for spherical particles from the experimental data of Mays and for EAM simulations using the Johnson and Trimble potentials.	41

Figure 4-2– Simulation results of overall spherical cluster relaxation, $\Delta r/r$, as compared to that expected for a mean pressure induced relaxation only, ϵ_a . Both the Johnson and Trimble potentials are shown..... 43

Figure 4-3 – Surface images of structures generated with the a) phase field model and the b) Berk model. 46

Figure 4-4 – Surface area calibration plot based on the number of surface atoms of unrelaxed spherical particles and spherical voids with known surface areas. 47

Figure 4-5 – Relaxation of nanoporous (NP) Au $\Delta L/L$ compared to that of the spherical clusters $\Delta r/r$, for both the Johnson and Trimble potentials. Also, plotted is the strain, ϵ_a in the center of the np-Au metal ligaments for the Johnson potential. The average ligament diameters for the nanoporous structures range from 12.8 to 17.6 Å..... 48

Figure 4-6 -- Surface images of the bicontinuous structures used in the simulations shown above..... 51

Figure 4-7 -- Shown here is the strain in spherical clusters as well as strain in periodic cubes with spherical voids versus surface area to volume ratio. 53

Figure 4-8 – Strain in spherical particles relaxed with MS and the Johnson potential calculated in two ways with two different definitions of the radius. 55

Figure 4-9 – Multilayer relaxation in spherical particles relaxed with the Johnson potential in the three directions (100), (110) and (111). 59

Figure 4-10 – Histogram of the number of number of atoms with a given value of the average nearest neighbor distance. This corresponds to the average local strain around a given atom..... 61

Figure 5-1 -- Porous gold created by the selective dissolution of Ag from a $Ag_{0.7}Au_{0.3}$ alloy in concentrated nitric acid. The sample was coarsened by a post dealloying heat treatment. The as-prepared ligament diameter can be as small as 3 nm..... 63

Figure 5-2 -- In Situ SANS data of dealloying. In Situ SANS data taken during the dealloying of $Ag_{0.7}Au_{0.3}$ in conc. Nitric Acid. Inset: Log-Log representation of Normalized SANS data showing the goodness of fit (red line) using the Berk model with the dispersion of wavevectors defined by the Schultz distribution ($z = 13$)..... 67

Figure 5-3 -- Simulated nanoporous gold. Simulated 3-d slice through a bicontinuous structure calculated using the Berk fit. The pixel resolution in the image above was on the order of an atomic Au radius..... 68

Figure 5-4 -- Relaxation curves for nanoporous gold. Volumetric strain for the 1.8 nm ligament sample after application of potentials Au1, Au2, Au3, and Au4 respectively. The value of the (111) unrelaxed surface stress is indicated on the figure for reference. The inset is a slice through the initial structure. 73

Figure 5-5 -- Mechanical instability of np-Au. Radial distribution function for several timesteps during the relaxation of the 1.8 nm diameter ligament sample with potential Au4 showing the transition to an amorphous structure. Inset shows the relaxed structure after 800 ps..... 76

Figure 5-6 -- Length measurement comparison between the bicontinuous structures generated by the phase field model as compared to those generated by the Berk model based on the distribution in wavelengths measured by small angle neutron scattering for dealloyed np-Au..... 79

Figure 5-7 -- Plastic deformation induced by surface stress values of 3.8 and 4.5 J / m² as indicated. The presence of stacking faults is indicated in the figures. 80

Figure 5-8 -- Critical surface stress to initiate plastic deformation versus the volume to surface area ratio. The points correspond to the samples with ligament diameters of 1.5, 1.8, 2.1, 2.7, and 3.6 nm. The samples with ligament diameters of 1.3 and 1.4 nm were unstable to all of the potentials of Table 5-1..... 81

Figure 5-9 – Radial distribution function for several timesteps during the densification of the 1.8 nm ligament size sample subjected to a surface stress of 6.3 J/m². The broadening and diminishing of the 2nd and 3rd neighbor shell peaks is indicative of amorphization. 83

Figure A-1-- Variations of bulk modulus B and lattice parameter a₀ (a), and formation energy of the alloy (b) as a function of Fe composition. Thin straight lines represent the linear interpolation corresponding to the ideal solution. Maximum departures for B and a₀ from ideal behavior are 2.5% and 0.1%, respectively..... 94

Figure A-2. Polynomial h(x) representing the composition dependence of the cross potential versus Fe composition, according to Equation (11)..... 95

Figure A-3. Short range order parameter versus Cr composition as calculated by Monte Carlo simulations with the new potential and experimental measurements from [11]..... 97

LIST OF TABLES

Table 3-1 – EAM parameters for Johnson and Trimble potentials.....	24
Table 3-2 – Fitting parameters for the Haftel potentials in order to adjust the embedding function to control the surface stress of the potential..	29
Table 4-1 – Average ligament diameters for porous structures calculated with chord lengths.....	52
Table 5-1 – Surface stress given by EAM potentials of Haftel, et al. Columns 2 & 3 give the values of the surface stress on the (100) and (111) surfaces taken from ref. 26 while column 4 gives the results of the isotropic surface stress for relaxed spheres.....	71
Table A-1 – Values of the Redlich-Kister expansion coefficients, Equation (5), corresponding to ΔH_{Fe-Cr}^{mix} from Rf. [6], in eV.....	93
Table A-2 – Coefficients of the 4th order polynomial h(x) in Equation (10, with values extracted from a global minimization as explained in the text.....	93

CHAPTER 1 Introduction

The technology of creating nanoporous metals through the corrosion process now referred to as dealloying has been utilized for several thousand years. The Inca of pre-Columbian South America used a process now known as depletion gilding to give an appearance of pure gold to dilute copper gold alloys[1]. The process of depletion gilding could be performed in either of two ways. The first method involves heat treating in an oxygen containing atmosphere (air) resulting in the formation of copper oxide on the surface. The oxide could then be removed by chemical dissolution. The second method involved the immersion of the alloy in a corrosive bath which would result in selective removal of the less noble element, Cu in this particular case, leaving behind a gold rich surface layer. This second method is what is now termed dealloying. The gold surface layer created by this process has a porous “sponge-like” microstructure. This porous surface layer could then be consolidated by burnishing.

The scientific understanding of this process and the resulting nanoporous structures has advanced over the years. The term dealloying (selective leaching) refers to the selective removal of one element of an alloy by corrosion processes [2]. In the particular case of a binary alloy this process results in the formation of a bicontinuous metal / void microstructure. A typical image of these bicontinuous structures is shown in Figure 1-1.

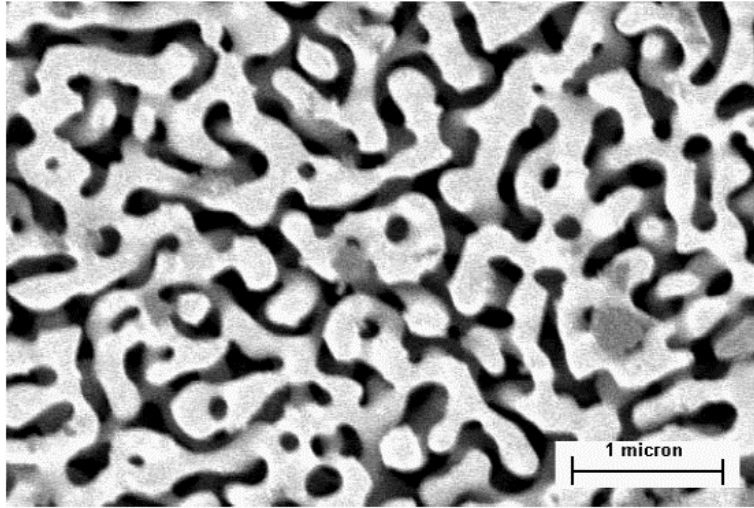


Figure 1-1 – Scanning electron micrograph of a nanoporous gold formed by dealloying.

These structures and their formation have been the focus of a great deal of research because they can be responsible for the stress corrosion cracking of several alloy systems[3-7]. Recent work in this area has been centered on utilizing this selective dissolution process to form nanoporous structures in which the size scale of the porosity and the distribution in pore sizes can be tailored by controlling the processing conditions[8]. The bicontinuous structures can be characterized with small angle neutron scattering and a characteristic length scale and pore size distribution for the structure can be extracted from the scattering curve [9]. The size scale of the porosity can be varied from ~5 nm-50 μm [10]. The small pore sizes of these materials yield very high surface area to volume ratios. For example, a 100 μm thick nanoporous foil with a pore size of 10 nm will have a surface area approximately 10,000 times that of a fully dense foil of the same size. Possible applications for these new materials are in the area of miniaturized electrodes for sensors[11] and actuators[12] owing to these high surface area to volume ratios.

Recent work has shown that nanoporous platinum formed by sintering of 6 nm particles can exhibit charge-induced reversible strain amplitudes ($>0.1\%$) comparable to those of commercial high-modulus piezoelectrics ($0.1-0.2\%$)[13]. The strains are isotropic in these nanoporous metals so the volumetric strain can be much larger than piezoelectrics. The strains are generated by adding or withdrawing charge at the surfaces. This causes a change in the surface stress thus introducing a strain in the material. The strain is a reaction to the changes in surface properties and is proportional to the surface area to volume ratio. More recently, the same effect has been demonstrated in nanoporous gold formed by selective dissolution[14]. The authors were able to achieve macroscopic bending of nanoporous gold cantilevers in an electrolyte by varying the electrochemical potential. This demonstrates the possibility of using these nanoporous metals formed by dealloying as actuators.

An issue of concern with the possible use of these materials in sensor and actuator applications is that they can exhibit brittle behavior and very little is known about their mechanical stability[15]. This behavior provided the motivation for our investigation of the mechanical stability of these materials at the atomistic level. This investigation will be the main topic of this dissertation. The size scales of these structures allowed us the possibility of simulating, atomistically, the behavior of “real-size” structures.

This document is divided into several chapters as follows. Chapter 2 contains background information as well as a brief review of the pertinent literature. Chapter 3 will describe the Embedded Atom Method (EAM) potentials used in this work as well as

a description of the development of a few EAM potentials for alloy systems. Chapter 4 is entitled Surface Stress Induced Strains in Nanoporous Au and consists of a paper submitted June 2006 to Nano Letters as well as some supplemental information. Chapter 5 is entitled Surface Stress Dependent Stability of Nanoporous Gold and consists of a paper submitted May 2006 to Nature of Materials.

CHAPTER 2 Background and Literature Review

In this section, background information related to the stability of nanoporous metals will be presented. The information will be divided into four sections: dealloying, surface stress and electrocapillarity, mechanical failure of porous materials and the embedded atom method. The section on dealloying will give a brief introduction into a method of forming nanoporous metals experimentally.

2.1 Dealloying

Dealloying is a corrosion process in which one component of an alloy is selectively removed[16]. In the case of a binary alloy this process results in the formation of a bi-continuous metal/void structure of the more noble element.

The first mention of this process in the scientific literature came from Calvert and Johnson in a work titled “The action of acids upon metals and alloys”[17] . They performed numerous experiments investigating the effects of various acids and their concentrations on several pure metals and binary alloys. They noticed this process of selective dissolution of the less noble element in the Cu-Zn alloy. In the case of a cube of $Zn_{0.5}Cu_{0.5}$ in a “weak nitric acid” for a period of 24 hours, all of the Zn was removed from the alloy leaving behind a cube of pure Cu with apparently the same dimensions as that of the original alloy.

In 1922, Moore made a link between the process of dealloying and a “real world” technological problem[18]. Brass cartridge casings for ammunition were stored in barns during these times. The cartridge casings were made of a $\text{Cu}_{30}\text{Zn}_{70}$ alloy. The ammonia in the environment of the barn would cause the selective removal of the Zn from the alloy. Then during the change in seasons the temperature changes would strain the casings as a result of thermal expansion/contraction. This strain would induce cracking in the cartridge casings. This process of dezincification of brass was then further investigated by Abrams[19].

Then, starting in the 1960's, Forty and Pickering providing the pioneering work looking into the electrochemical aspects of the dealloying process[20-22]. They were the first to look at polarization curves for this process and they first presented the idea of a critical potential for dealloying. They also started to investigate the morphology of these structures and made the link between the formation of these porous structures and stress corrosion cracking.

Sieradzki and Newman first proposed a fundamental description of the dealloying process in 1987 [23]. They described the dealloying process as a competing process of surface roughening and surface smoothening[24, 25]. The dissolution of the less noble element results in a roughening of the surface. Then transport processes (surface and

bulk diffusion of the more noble element) result in smoothening of the surfaces as well as cluster formation and growth.

More recent work in the area has been involved with tailoring of the microstructures electrochemically through varying the processing conditions. The size scale of the structure can be dependent on the applied dealloying potential[26], electrolyte composition[27] as well as post dealloying heat treatment[15].

There has also been continued work on trying to develop an understanding of the dealloying process. In this effort a kinetic Monte Carlo model was developed to simulate Ag-Au dealloying[10]. This model included only diffusion of silver and gold and dissolution of silver. They found this model was sufficiently able to reproduce all relevant kinetic and morphological experimental trends that are characteristic of dealloying.

The requirements for this process to occur are basically twofold[9]. First, the metal/metal ion electrode potentials of the two components must have a considerable difference. This difference results in different rates of anodic dissolution for the two constituents.

Therefore a potential can be applied at which the less noble element readily dissolves while the more noble element remains stable. The second requirement is that the concentration of the less noble element in the alloy must be greater than a critical value. If this is not the case, the less noble element will be leached out of the first few atomic

layers on the surface resulting in an enrichment of the more noble element thereby passivating the surface and stopping the dealloying process from continuing.

The average pore size and the pore size distribution of the structure will depend upon the electrolyte composition, de-alloying rate, applied potential and time. Therefore, the morphology of the structure can be tailored for specific applications by controlling these processing conditions.

2.2 Surface Stress and Electrocapillarity

In recent work by Gleiter[28], it was proposed that nanometer sized structures may provide a way to create solids with tunable properties. This tunability can be achieved through the application of applied external or internal electric fields. These fields can affect the charge carrier density of the surface and interface regions of a material. The local deviations from charge neutrality result in locally modified properties such as phase equilibria, magnetic properties and surface stresses. In the case of nanometer-sized structures, these locally modified properties can result in changes in macroscopic properties as a result of the surfaces composing a significant volume fraction of the material.

A simple example of the space-charge region induced by an external voltage follows[28]. Figure 2-1 is a schematic showing a simple capacitor in which two chemically identical, semi-infinite crystals with plane parallel surfaces are separated by a gap of width d . The

gap is filled with a material with dielectric constant, ϵ . If a voltage, U , is applied between the two materials, the charge density per unit area, q , transferred between the two is given by,

$$q = \epsilon_0 \epsilon \frac{U}{d},$$

where ϵ_0 is the dielectric constant of a vacuum and δ is the electric screening length

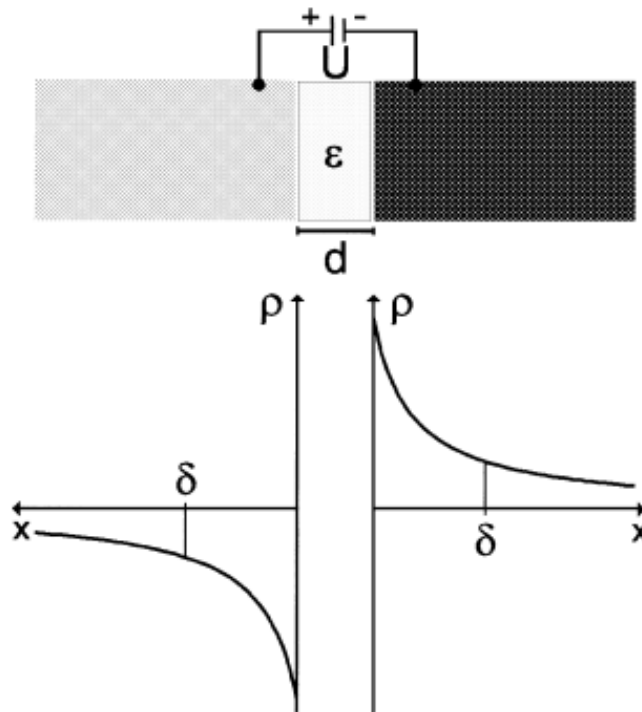


Figure 2-1 -- Charge density ρ in semi-infinite crystals adjacent to an insulating interface (thickness d , relative dielectric constant ϵ) upon applying a voltage U , δ : screening length[28]. Reprinted with permission from Elsevier.

The charge density per unit area is limited by the breakthrough strength and the dielectric constant. Large values of q can be obtained when a voltage is applied to a metal in contact with an electrolyte. In aqueous electrolytes, the double-layer capacitance of a

clean metal surface is typically 15-30 $\mu\text{F}/\text{cm}^2$. This can support voltages up to 1.2V and

gives, $q \leq 0.3 \frac{As}{m^2}$.

Of particular interest in our research is the modification of the surface stress of a metal through the application of an electric field. There are two fundamental excess thermodynamic quantities of a surface: surface free energy (γ) and surface stress (f).

The surface free energy is defined as the reversible work per unit area to form a new surface while keeping a constant equilibrium density of surface atoms. The surface stress is the reversible work per unit area required to form a new surface by elastic deformation of a preexisting surface. The surface stress in general is a tensor quantity and is expressed by the Shuttleworth equation,

$$f_{ij} = \gamma \delta_{ij} + \frac{\partial \gamma}{\partial \varepsilon_{ij}},$$

where δ_{ij} is the Kronecker delta and ε_{ij} is the surface strain tensor[29]. If a surface has a 3-fold or higher rotation axis of symmetry, the surface stress is isotropic and f is a scalar. The surface stress is generally of the same order of magnitude as the surface free energy and can be either positive or negative.

In the case of a fluid undergoing elastic deformation, new atoms go to the surface thereby maintaining, on average, a constant density of surface atoms. Therefore $f \equiv \gamma$ for fluids.

However, in solids the elastic deformation results in a change in the number of surface

atoms per unit area and $f \neq \gamma$. The surface stress is a difficult quantity to measure experimentally. There are two methods typically used to determine surface stress, lattice parameter measurements as a function of particle size and wafer curvature methods.

The Gibbs adsorption equation appropriate for the solid/electrolyte interface[13] is

$$d\gamma = -sdT + 2(f - \gamma)d\varepsilon - qdV - \sum_i \Gamma_i d\mu_i,$$

where T is the temperature, ε is the linear elastic strain, μ_i is the chemical potential of species i , s is per unit area, Γ_i are surface excesses of entropy, V is the electrochemical potential, and q is the charge. At constant T and μ_i the electrocapillarity equation for solid electrodes is given as

$$\left(\frac{d\gamma}{dV} \right)_{T, \mu_i} = -q + 2(f - \gamma) \left(\frac{d\varepsilon}{dV} \right)_{T, \mu_i}.$$

The first measurements of the change in surface stress with applied potential were reported by Lin and Beck[30]. The change in the surface stress will induce a strain in the plane of the surface. They used a sensitive extensometer technique to then measure the extension of long thin polycrystalline gold ribbons as a function of the applied electrochemical potential. A typical value for the change in surface stress with applied potential for a Au (111) surface is 0.5 J/m^2 for a 0.5 V change in potential. The change in charge density for the same 0.5 V change is 0.1 C/m^2 [31].

This surface stress induced strain effect has recently been shown to provide reversible strain amplitudes, in nanoporous platinum formed by sintering, that are comparable to commercial piezoelectric materials[13]. The platinum samples were formed by consolidation of commercial Pt black with a grain size of 6 nm. The samples were then immersed in aqueous electrolytes and the strain was measured as a function of the applied potential. Reversible linear strain amplitudes in excess of 0.1% were observed. The strain in these materials is isotropic; therefore the volumetric strain achieved was approximately 0.45%.

The same effect has also been demonstrated with nanoporous gold formed by dealloying [14]. In this particular case bilayer foils were created to exhibit visible macroscopic bending of cantilevers. The foils were generated by mechanically bonding a Ag-Au alloy foil to a pure Au foil by cold rolling. The resulting structure was a bilayer of 6 μm thick Au and 24 μm thick Ag-Au. The bilayer foil was then dealloyed in 1M perchloric acid to remove the Ag from the Ag-Au layer leaving behind a nanoporous Au layer on a fully dense Au substrate. Then by applying a potential electrochemically between two of these foils they observed reversible macroscopic bending of the cantilevers. This results from the change in surface stress that is induced by the changing electrochemical potential and since the nanoporous Au has such a high surface area to volume ratio, the effect is quite pronounced in comparison to the fully dense gold substrate. This results in a bending due to the unbalanced surface stresses in the two layers.

A relationship describing the interface induced stress in solid microstructures has been developed by Weismuller and Cahn [32]. This generalized capillary equation is given as

$$3V \langle \Delta P \rangle_V = 2S \langle f \rangle_S,$$

with $\Delta P = P - P_{ext}$, where V is the volume, S is the surface area and f is the surface stress, $\langle \Delta P \rangle_V$ is the volume averaged pressure and $\langle f \rangle_S$ is the area averaged surface stress. This relationship applies irrespective of the specific geometry of the microstructure and can be therefore used to predict the pressure in the nanoporous structures induced by the surface stress. The pressure results in an elastic strain of the solid through the bulk modulus. The generalized capillary equation reduces to the

Laplace equation for the case of a sphere where $\frac{S}{V} = \frac{3}{r}$.

2.3 Mechanical Failure of Porous Materials

Since the ability of these nanoporous metals to perform as sensors/actuators has been demonstrated, the understanding of their mechanical stability will be quite important in terms of practical applications. These materials, (Pt and Au for example) are quite ductile in their fully dense form whereas they can be quite brittle in the nanoporous form.

Much theoretical/computational work has been done in the area of fracture in random porous structures [33-36]. An important prediction resulting from this work is of a ductile-brittle transition that depends on the ratio of the sample size to the distribution of element strengths[35]. Li and Sieradzki have demonstrated this effect experimentally for

random porous gold[37]. They performed three-point bend tests to failure with specimens of constant size and varying pore size distributions. The tests were performed under displacement control. In their treatment of the results, it was assumed that there was no microscopic ductile to brittle transition as a function of the ligament size. That is to say that the ligaments do not become inherently brittle as the size of the ligament becomes small. The ligament size distribution would then be proportional to the distribution in element strengths.

A dealloyed film on the surface of silver-gold alloys has been shown to induce intergranular cracking in the undealloyed region of the material[38]. In this study, 69 μm thick Ag-Au foils were dealloyed to create porous surface layers of varying thickness. Tensile tests were then performed to determine the susceptibility to film induced cracking. It was found that films of 10-20 nm were capable of inducing a cleavage event. Films thicker than 3 μm resulted in 100% brittle intergranular fractures.

2.4 Classical Atomistic Simulations

2.4.1 Molecular Statics (MS)

In this work the term Molecular Statics (MS) will be used to describe simulations in which a standard conjugate gradient technique[39] is used to find a local minimum in the total energy of a system of atoms at a temperature of 0K. This minimization scheme is an iterative process in which the atoms are moved in the direction of the steepest gradient in

the energy function until a local minimum in the total energy is located. A FORTRAN code developed by Dr. Yuri Mishin was used to perform the MS energy minimizations in this work. This code allows for local atomic relaxations as well as a uniform isotropic deformation of the simulation block. Embedded atom method potentials were used to describe the atomic interactions in these simulations.

2.4.2 Molecular Dynamics (MD)

“An intelligence which could, at any moment, comprehend all the forces by which nature is animated and the respective positions of the beings of which it is composed, and moreover, if this intelligence were far-reaching enough to subject these data to analysis, it would encompass in that formula both the movements of the largest bodies in the universe and those of the lightest atom: to it nothing would be uncertain, and the future, as well as the past, would be present to its eyes. The human mind offers us, in the perfection which it has given to astronomy, a faint sketch of this intelligence [40]. “

In this famous quote of Laplace, he has set forth the basic concept of molecular dynamic simulations. Molecular dynamics simulations are used to estimate equilibrium and dynamic properties of complicated systems that can not be solved analytically. These simulations provide a link between theory and experiment. They are essentially an integration of Newton’s equations of motion through which the positions and velocities of a system of particles can be followed as a function of time.

Newtonian Dynamics

In principle this is a very simple method [41]. The motions of a system of particles under an applied force field are simulated by tracking the motions in time according to

Newton's second law given as,

$$\vec{F}_i = m\ddot{\vec{r}}_i,$$

where i is a spherical particle, m is the mass of that particle, \vec{r}_i is the position vector of particle i with respect to a fixed set of axes, and \vec{F}_i is the force exerted on particle i .

The velocity of the particle i is given as

$$\vec{v}_i = \frac{d\vec{r}_i}{dt}$$

and the acceleration of the particle is given as,

$$\ddot{\vec{r}}_i = \frac{d^2\vec{r}_i}{dt^2}.$$

If the force exerted on the particle is zero, the velocity of the particle will remain constant, this is Newton's 1st law. Newton's 3rd law can also be derived from this set of equations for the case of an isolated system of two spherical particles. An isolated system by definition has no external forces acting upon it and

$$F_{total} = 0.$$

The sum of the force exerted on particle 1 by particle 2 and the force exerted on particle 2 by particle 1 must be zero,

$$F_{total} = F_1 + F_2 = 0,$$

therefore,

$$F_1 = -F_2 .$$

The kinetic energy is then the amount of work required to move a spherical particle initially at rest to a velocity \dot{r} and is given by

$$E_K = \frac{1}{2} m \dot{r}^2 .$$

Hamiltonian Dynamics

Since the form of Newton's 2nd law is independent of time, there should exist some function of the positions and velocities that is time independent as well. This function is the Hamiltonian and is defined as

$$H(r^N, p^N) = \text{const}$$

where the particle momentum, p_i , is given as the product of the mass and velocity of the particle

$$p_i = m \dot{r}_i$$

In the case of an isolated system the total energy, the sum of the kinetic and potential energies of the individual particles, is conserved.

$$H(r^N, p^N) = \frac{1}{2m} \sum_i p_i^2 + U(r^N) = E$$

where U is the potential energy function resulting from interparticle interactions.

The total time derivative of the general Hamiltonian is shown as,

$$\frac{dH}{dt} = \sum_i \frac{\partial H}{\partial \vec{p}_i} \cdot \dot{\vec{p}}_i + \sum_i \frac{\partial H}{\partial \vec{r}_i} \cdot \dot{\vec{r}}_i + \frac{\partial H}{\partial t}$$

Since H is not explicitly a function of time we have

$$\frac{dH}{dt} = \sum_i \frac{\partial H}{\partial \bar{p}_i} \cdot \dot{\bar{p}}_i + \sum_i \frac{\partial H}{\partial \bar{r}_i} \cdot \dot{\bar{r}}_i = 0$$

In the case of an isolated system the total time derivative of Equation is

$$\frac{dH}{dt} = \frac{1}{m} \sum_i \bar{p}_i \cdot \dot{\bar{p}}_i + \sum_i \frac{\partial U}{\partial \bar{r}_i} \cdot \dot{\bar{r}}_i = 0$$

Comparison of the above two equations yields,

$$\frac{\partial H}{\partial \bar{p}_i} = \frac{\bar{p}_i}{m} = \dot{\bar{r}}_i$$

and

$$\frac{\partial H}{\partial \bar{r}_i} = \frac{\partial U}{\partial \bar{r}_i}$$

Substituting equation into equation gives

$$\sum_i \dot{\bar{r}}_i \cdot \dot{\bar{p}}_i + \sum_i \frac{\partial H}{\partial \bar{r}_i} \cdot \dot{\bar{r}}_i = 0$$

$$\sum_i \left(\dot{\bar{p}}_i + \frac{\partial H}{\partial \bar{r}_i} \right) \cdot \dot{\bar{r}}_i = 0$$

therefore

$$\frac{\partial H}{\partial \dot{\bar{r}}_i} = -p_i$$

Equations and are Hamiltonian's equations of motion. They represent a system of 6N first order differential equations as opposed to Newton's equations of motion which consist of a series of 3N second order differential equations.

The basic MD simulation method involves the following steps: Initialization, Equilibration and Production. First, the initial conditions must be specified. This includes the specification of initial particle positions and velocities. The initial velocities are typically set pseudorandomly in order that the total kinetic energy corresponds to the value expected at the initial temperature of the simulation. At thermal equilibrium, each normal vibration mode has on average $(k_B T)/2$ energy, where k_B is the Boltzmann constant and T is the temperature.

$$\langle E_k \rangle = \frac{1}{2} \sum_{i=1}^{3N} m_i v_i^2 \equiv \frac{1}{2} (V^0)^T M (V^0) = (N_F k_B T) / 2$$

This is achieved by setting the velocity components from a Gaussian distribution.

Once the initial coordinates and velocities are assigned, the equilibration phase can begin. In this stage there is an exchange between kinetic and potential energy. The equilibration is complete when there is convergence of both the kinetic and potential energies with small fluctuations occurring about the mean value. This is the behavior that is expected for a microcanonical ensemble, fixed total particle number, volume and energy (NVE). Other MD ensembles include canonical, constant temperature and volume (NVT), isothermal-isobaric, constant temperature and pressure (NPT), and constant pressure and enthalpy (NPH). In this work the molecular dynamics simulations were performed using the NPT ensemble.

Lastly, we can begin the production phase in which external forces or constraints can be applied to the system and the evolution of the positions and velocities can be followed.

2.4.3 Embedded Atom Method (EAM)

The utilization of atomistic simulations in materials science is increasing due to the constantly increasing speed of computers. The accuracy of the predictions made by such a simulation can only be as good as the model used to describe the interactions between atoms. The embedded atom method (EAM) is a semi-empirical model for describing these interactions. The EAM model scales with the number of atoms, n , and therefore allows simulations with much larger numbers of atoms than simulations based on first principles which scale as n^3 or higher.

The embedded atom method considers each atom to be embedded in a host lattice consisting of all other atoms in the simulation block[42]. In the EAM formalism for a pure metal, the total energy of a system of n atoms is given by the sum over atom energies,

$$E_{tot} = \sum_i^n E_i .$$

The energy of an atom, E_i , is composed of two terms and is given by,

$$E_i = \frac{1}{2} \sum_j \phi(r_{ij}) + F(\bar{\rho}_i) .$$

The first, ϕ , is the electrostatic pairwise interaction between atoms and is a function of the scalar distance between them, r_{ij} . The second term is the so-called “embedding energy”.

The ‘embedding function’, F , is a function of the local electron density,

$$\bar{\rho}_i = \sum_j \rho(r_{ij}) ,$$

into which the atom is being ‘embedded’. The density function, ρ , is also a pairwise interaction term that is a function of the scalar distance between atoms. The pairwise interactions, ϕ and ρ , are typically limited to 1 to 5 coordination shells in the perfect lattice. This cutoff is chosen to balance the computational speed with the flexibility in the functions to fit desired material properties.

The exact forms of the three functions, ϕ , ρ and F are not known and must then be parameterized. The coefficients of the parameterized functions are determined by fitting to known material properties. These properties include lattice parameter, cohesive energy, elastic constants as well as defect properties such as surface energies and vacancies.

CHAPTER 3 Atomistic Simulations Methods

This chapter is divided into two main sections. The first section describes the EAM potentials for Au which were used in this work including those of Johnson, Trimble and Haftel. The second section explains the method used to develop EAM potentials for a few alloy systems.

3.1 EAM Potentials for Au

3.1.1 Johnson and Trimble Potentials

For our work, the EAM potentials for Au of both Johnson [43] and Trimble [44] were selected in order to look at the effect of varying surface stress on the relaxation and deformation behavior of the nanoporous samples. Johnson's potential is an analytical model for the potential functions, ϕ , ρ and F . Trimble's potential is a modification of the Johnson potential in order to adjust the surface energy and surface stress to more closely fit experimental and first principles data and also to stabilize the reconstruction of the (111) surface.

Johnson uses different variables in the EAM formalism as follows

$$E_{tot} = NE \text{ ,}$$

$$E = F(\rho) + \frac{1}{2} \sum_m \phi(r_m) \text{ ,}$$

$$\rho = \sum_m f(r_m) \text{ ,}$$

with N being the number of atoms, E the energy per atom and r_m the m^{th} neighbor to a particular atom.

The electron density function,

$$f(r) = f_e \exp\left[-\beta\left[\frac{r_1}{r_{1e}} - 1\right]\right], \quad r \leq r_c,$$

and the pair potential,

$$\phi(r) = \phi_e \exp\left[-\gamma\left[\frac{r_1}{r_{1e}} - 1\right]\right], \quad r \leq r_c,$$

are both represented by a single exponential term. The embedding energy, $F(\rho)$, is given by

$$F(\rho) = -E_c \left[1 - \frac{\alpha}{\beta} \ln\left[\frac{\rho}{\rho_e}\right]\right] \left[\frac{\rho}{\rho_e}\right]^{\alpha/\beta} - \Phi_e \left[\frac{\rho}{\rho_e}\right]^{\gamma/\beta}$$

with

$$\rho_e = 12f_e,$$

$$\Phi_e = 6\phi_e,$$

and

$$\alpha = 3 \left[\frac{\Omega_e B_e}{E_c} \right]^{1/2}$$

where Ω_e is the atomic volume, B_e is the bulk modulus and E_c is the cohesive energy.

This leaves four adjustable parameters in the model, ϕ_e, β, γ and r_c assuming that the cohesive energy and the bulk modulus are fit exactly. The exact value of the cutoff, r_c ,

has little effect on the results as long as it is not too close to a given coordination shell radius.

The parameters for the Johnson and Trimble potentials are shown in Table 3-1. The functions are plotted in Figure 1-3.

Table 3-1 – EAM parameters for Johnson and Trimble potentials

	Johnson	Modified
α	6.365	6.55
β	6	4.7
γ	10.1	9.0
φ_e	0.2082	0.22843

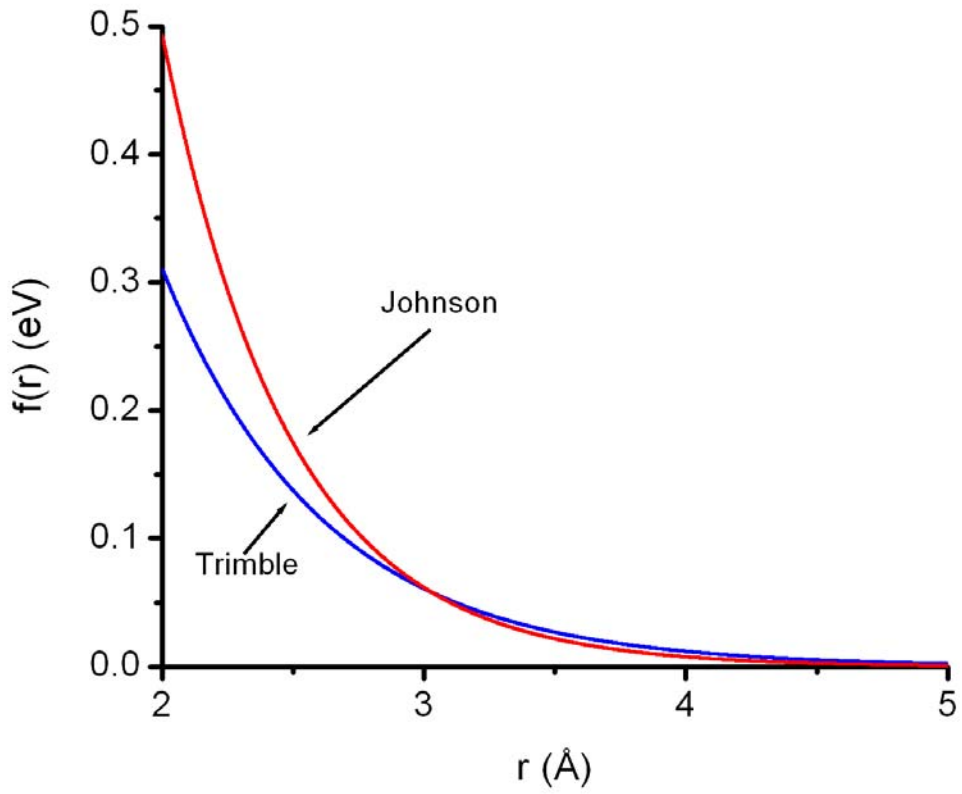


Figure 3-1 – Electron density function $f(r)$ for the Johnson and Trimble potentials in the effective pair format.

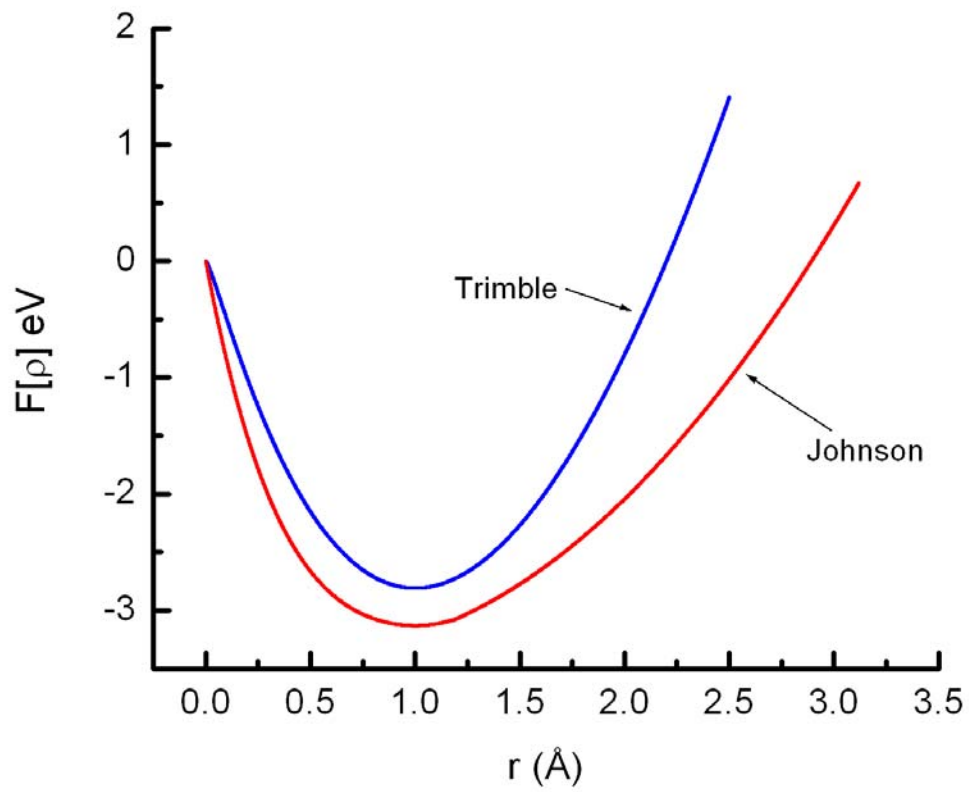


Figure 3-2 Embedding functions $F(\rho)$ for the Johnson and Trimble potentials in the effective pair format.

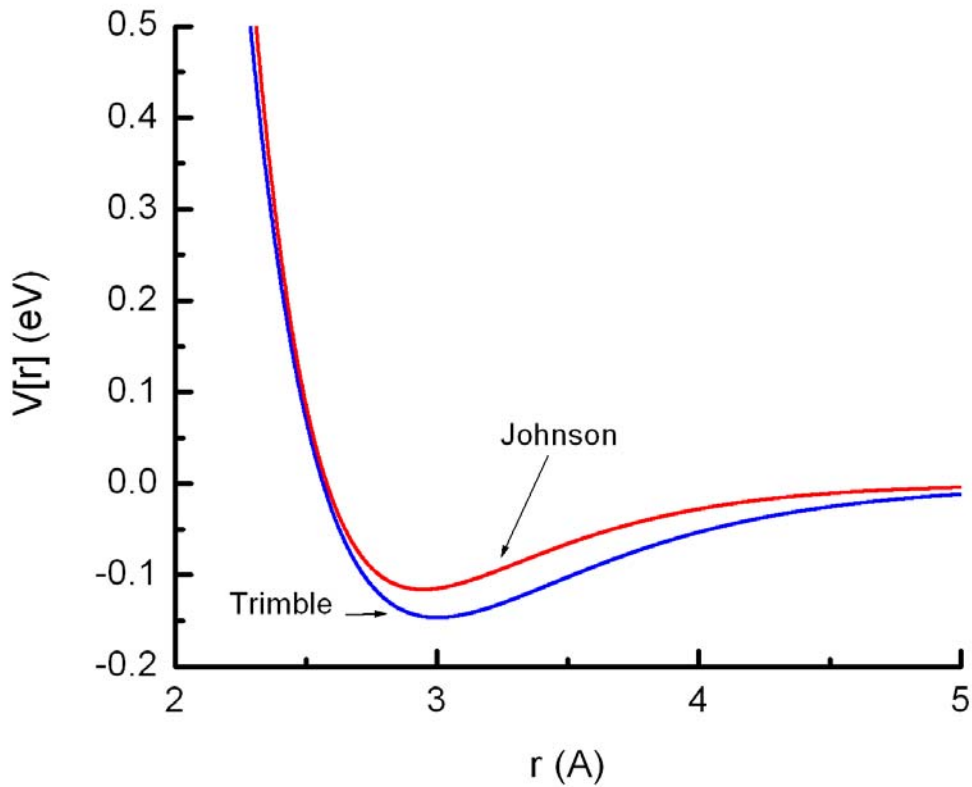


Figure 3-3 – Pair potential functions $V(r)$ for the Johnson and Trimble potentials in the effective pair format.

The Trimble potential demonstrates the possibility of varying the surface stress predicted by the Johnson potential by adjusting the fitting parameters in the model. This seems to work quite well in stabilizing the reconstruction of the gold (111) surface. An issue of concern, when using this potential, is that the adjustment of the parameters has small effects on other properties, most importantly the bulk modulus.

3.1.2 Haftel and Rosen Potentials

Haftel and Rosen have presented a method for generating Au potentials with varying values of the surface stress[45]. They start with the Au potential of Ercolessi et al.[46] shown below.

$$V(r) = \sum_i a_i \left(\frac{r}{r_c} \right)^6$$

$$\Phi(r) = \Phi_0 (r - r_c)^6$$

$$F_0(\rho) = b_0 \rho + (b_1 \rho + b_2 \rho^2 + b_3 \rho^3) \ln \rho$$

Where $V(r)$ is the pair potential, $\Phi(r)$ is the electron density function, a_i are fitting parameters, r is the radius, r_c is the cutoff, ρ is the sum of the electron densities over the neighboring atoms, and b 's are also fitting parameters. Insert table of fitting parameters.

They maintain the original pair potential and electron density functions, $V(r)$ and $\Phi(r)$.

The variation of the surface stress is achieved by adjusting the embedding energy function at electron densities typical of surfaces (70-85% that of the bulk).

$$F_1(\rho) = F_0(\rho) + C|\rho - 1|^\alpha.$$

$$F(\rho) = \rho(A \ln \rho + B) \quad (\rho \leq \rho_m)$$

$$= F_1(\rho) \quad (\rho > \rho_m)$$

Since the embedding function is adjusted only for these non-equilibrium values of the electron density, the bulk properties predicted by these potentials remain the same. A series of 5 EAM potentials was created in which the (111) and (110) values of the surface

stress were systematically increased. The parameters, A, B and C, for the set of potentials are shown in Table 3-2.

Table 3-2 – Fitting parameters for the Haftel potentials in order to adjust the embedding function to control the surface stress of the potential.

	C	A	B
Au1	9	0.108527	-3.466118
Au2	30	0.78902	-3.379011
Au3	18	1.627345	-3.274483
Au4	15	1.834456	-3.248351
Au5	8	2.317713	-3.187377

3.2 EAM for Alloys

This section describes a method that was developed in order to create EAM potentials for concentrated alloys. This work was done in collaboration with Lawrence Livermore National Laboratory in order to develop a better understanding of the EAM through working with experts in this field. This work is not directly related to the main topic of this dissertation but provided some of the foundational understanding for this work.

The EAM formalism for alloys is very similar to that for the pure elements. We need to have definitions of the three functions for the pure elements, as well as additional terms for the mixed interactions are needed to define the potential. In the case of a binary alloy the total energy is defined as

$$E = \sum_i^N \left[F_{\alpha_i} \left(\sum_{j \neq i} \rho_{\alpha_i \beta_j}(r_{ij}) \right) + \frac{1}{2} \sum_{j \neq i} V_{\alpha_i \beta_j}(r_{ij}) \right]$$

where α and β denote the two elements composing the binary system, ρ is the electronic density function, V is the pair potential and F is the embedding function.

Prior research using the embedded atom method for alloys has focused on either ordered intermetallic phases or solid solutions in the dilute limits. Our focus was on extending this to fit alloy properties for solid solutions over the entire range of composition

3.2.1 Ta-W

The first system that was investigated was that of Ta-W. The phase diagram for Ta-W shows complete solid solution over the entire composition range. This system was expected to be relatively simple to fit because of this relatively uncomplicated phase diagram. This system is of some interest to the nuclear research community because it has some similar behavior to the Pu-Ga system. In recent work by Turchi et. al, [47] a phase diagram was predicted from first principles calculations that shows a slight tendency toward ordering (B2 phase) in this system at low temperatures. An asymmetry in the energy of mixing was also predicted, Figure 3-5.

The goal of our work on this system was to develop an EAM potential for Ta-W that could capture these features of the phase diagram.

The EAM energy expression is composed of two parts, a linear pair potential term and a non-linear embedding energy part. In order to build up the asymmetry in the mixing energy without altering the pure element functions we can use one of two methods:

1. Use a mixed pair density term, $\rho_{\alpha\beta}$, in order to take advantage of the non-linearity already present in the embedding function.
2. Make the mixed pair potential a function of the local composition.

In the case of Ta-W there is just a slight asymmetry in mixing energy so the first attempt was to generate a mixed density term in order to utilize the non-linearity already present in the embedding function. For the pure element potentials, we chose the Finnis-Sinclair N-body potentials because they are the most widely used in the literature[48]. The asymmetry in the mixing energy and the tendency to order were fitted using a cross density term, however there was a problem with the cutoff for the W potential that results in a discontinuity in the bulk modulus, Figure 3-4, that severely limits the use of this potential to composition ranges away from the discontinuity.

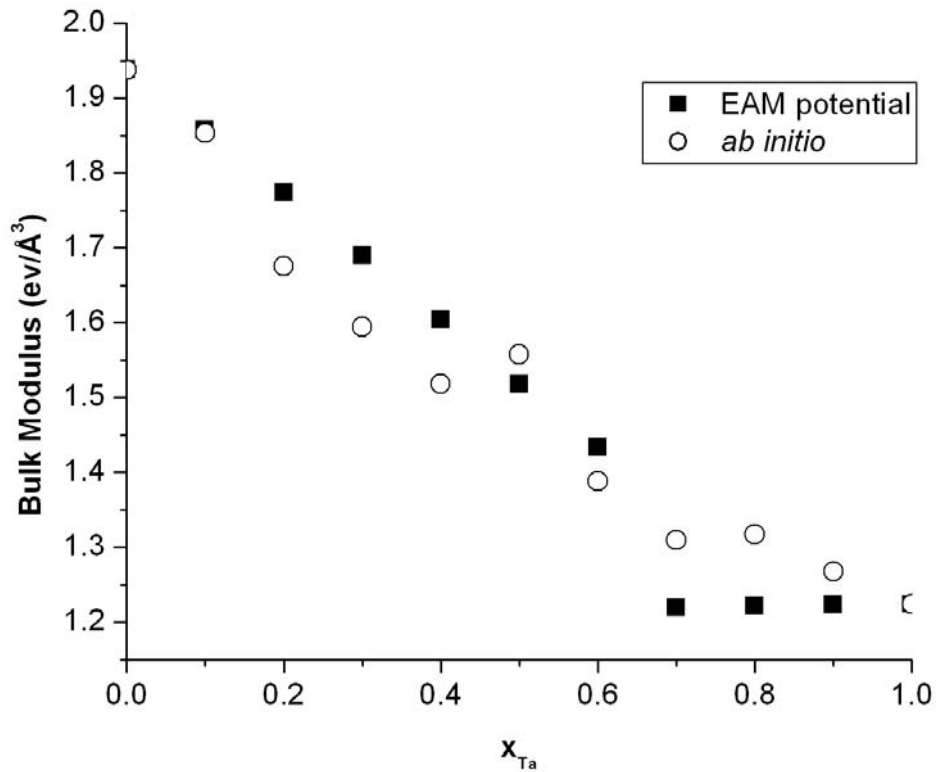


Figure 3-4 --Bulk Modulus (eV/Å³) vs. Concentration (Ta) Blue dots are the *ab initio* results and Red dots are the EAM fit

A point to note is that there seems to be an incompatibility between asymmetry in the mixing energy and the deviation from ideal mixing of the bulk modulus. That is to say that negative deviations from ideality are for both the mixing energy and the bulk modulus are predicted from first principles. This effect cannot be predicted from the EAM potential model.

3.2.2 Fe-Cr

Another system of interest was that of Fe-Cr. This system is of interest in fusion technology as a structural material with good mechanical, thermal and radiation properties.

In this system the phase diagram is more complex. Of particular interest is the ferromagnetic bcc Fe-Cr alloys ($T < 1000\text{K}$). Recent *ab initio* calculations predict a formation energy that exhibits a sign inversion at a Cr concentration of 0.94[49]. The formation energy can be described by a 4th order Redlich-Kister polynomial,

$$\Delta H(x) = x(1-x) \sum_{p=0}^n L_p (1-2x)^p,$$

where x is the concentration and L_p is the p^{th} -order binary interaction parameter, Figure 3-5.

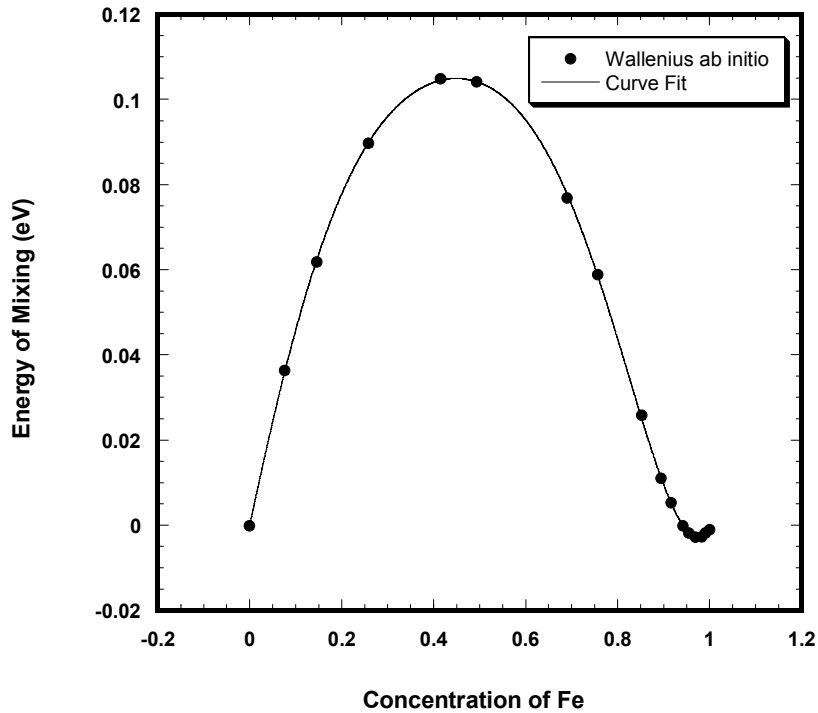


Figure 3-5 --Redlich-Kister fit to ab initio prediction of mixing energy for Fe-Cr.

In order to generate an EAM potential that can fit this complex formation energy, the mixed pair potential was defined as being a function of the local composition,

$$v_{AB}(x, r) = h(x) \frac{1}{2} (v_A(r) + v_B(r)),$$

where x is the composition, v_A and v_B are the pair potential functions of the pure elements and h is an arbitrary function of the local composition determined by a fitting procedure.

A plot of the function h is shown in Figure 3-6.

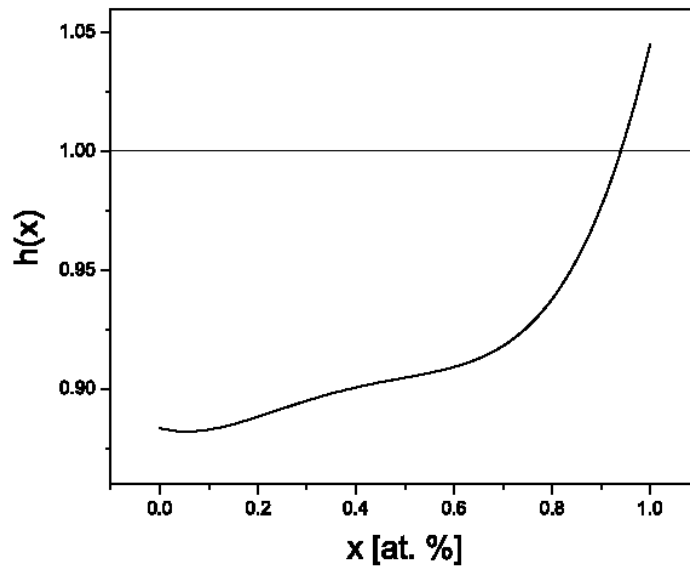


Figure 3-6 -- The function $h(x)$ determined from fitting the ab initio formation energy for Fe-Cr[50]

Although the fitting in this case was done only considering the formation energy, the potential yields very reasonable values for the bulk modulus and lattice parameter vs. composition, Figure 3-7.

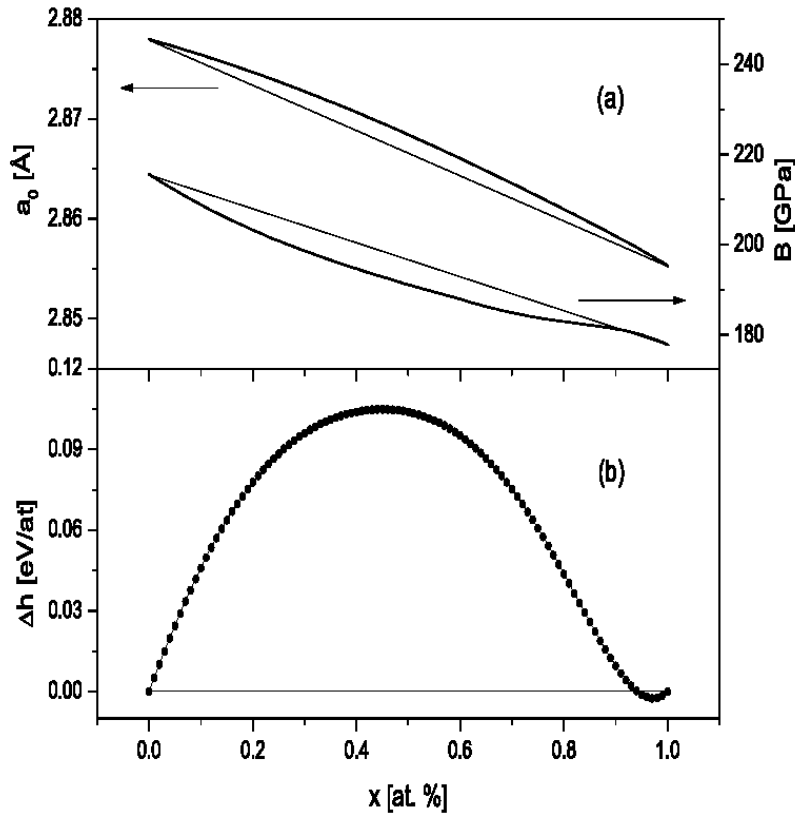


Figure 3-7 -- Lattice parameter, bulk modulus and formation energy predicted by the new EAM potential[50]

In order to use this new potential, simulation codes must be modified to calculate the local composition to determine the value of the mixed pair potential.

A paper entitled “Classical Many-Body Potential for Concentrated Alloys and the Inversion of Order in Iron-Chromium Alloys”, published in Physical Review Letters [50], detailing the method and results for the Fe-Cr case can be found in Appendix A.

CHAPTER 4 Surface Stress Induced Strains in Nanoporous Au

This Chapter is written in the form of a paper that was submitted to Nano Letters (4.1) along with some pertinent supplemental information (4.2).

4.1 Geometric Relaxation of Nanoporous Metals: Role of Surface Relaxation

Atomic scale computer simulations are used to probe the dominant mechanisms for the geometric relaxation of bicontinuous nanoporous (np) metals. We present a method for creating digital samples amenable to atomic simulations that are quantitatively similar to those prepared experimentally. Simulated relaxations of these structures, as well as the relaxation of model spherical clusters, indicate that the surface relaxation effect dominates the overall dimensional relaxation of np-metals post processing. Capillary effects play a secondary role in the overall relaxation.

PACS numbers: 68.35.Gy, 68.47.De, 82.45.Yz

Bicontinuous nanoporous (np) metals can be created through an alloy corrosion process referred to in the literature as selective dissolution or dealloying [51]. These structures, and their formation, have been the focus of a great deal of research since the acceptance of their role in the stress corrosion cracking of several alloy systems [52-56]. More recent, the ease of tailoring the average pore diameter [57, 58] coupled with the extremely high surface area to volume ratio for these materials has resulted in an interest for such applications as actuators [13], sensors [11], catalysts [59], heat exchangers [60],

and as skeletal structures in fundamental studies [61]. Actuation of these materials is a result of the electrocapillary effect whereby the surface stress in an electrochemical environment is a function of the applied potential [62]. Both np-platinum and np-gold have been shown to exhibit this behavior with strain amplitudes comparable to those of commercial high-modulus piezoelectrics [13, 14]. The actuation of these materials has been treated recently by Weissmuller and Kramer [63].

In this letter we are not concerned with the actuation of an existing np-metal structure but rather the relaxation that occurs during the creation of such a structure. That is, “If we start with an alloy of Ag-Au with edge length, L , and then remove the Ag from the alloy by selective dissolution, what governs the final dimension, L^* , of the resultant np-Au structure?” Our first inclination is to calculate the mean pressure within the np-metal ligaments through the generalized capillary equation [64] and then use the bulk compressibility to calculate the elastic strain. *However, we show in this paper that in fact the geometric volume change is not dominated by the mean pressure but rather by the surface relaxation effect (referred to as surface stretch in the literature).* We believe these results to be critical for an understanding of in-situ device fabrication as well as the induced stresses in stress corrosion cracking systems. These results are also of general interest to the understanding of stress generation in nanoscale technologies and general surface relaxation phenomena.

Simulations using the embedded atom method (EAM) have been shown to be quite useful in understanding phenomena on the atomistic scale and in particular, properties of

materials with nano-scale features [65]. In this Letter, the EAM potentials for Au of both Johnson [43] and Trimble [44] were selected. Johnson's potential consists of a set of analytical expressions for the potential functions. The Trimble potential is a modification of the Johnson potential whereby the surface energy and surface stress are adjusted to more closely fit experimental and first principles data as well as to stabilize the reconstruction of the (111) surface.

The surface stress (f) is a thermodynamic quantity which quantifies the energy needed to create new surface area by straining an existing surface. Whereas, the surface free energy (γ) quantifies the creation of new surface area by a process such as cleavage

[66]. In the isotropic case, the surface stress is given by: $f = \gamma + \frac{\partial \gamma}{\partial \varepsilon}$. Surface stress

values of gold have been experimentally determined by Mays [67]. In this method, gold nuclei of varying size were deposited onto an amorphous carbon substrate by evaporation. Assuming that the nuclei are spherical with an isotropic surface free energy, the hydrostatic pressure (ΔP) acting on the nuclei due to the surface stress is given by

the Laplace-Young equation, $\Delta P = \frac{2f}{r}$ where r is the radius of the nuclei. The

hydrostatic pressure induces an elastic strain (ε_a) given by Hooke's law,

$$\Delta P = -3K\varepsilon_a. \quad (1)$$

where K is the bulk modulus. These two preceding equations lead to an expression for the isotropic surface stress as a function of the particle radius:

$$f = -\frac{3K\varepsilon_a r}{2}. \quad (2)$$

Mays measured the lattice parameter of Au particles as a function of radius, r , in the TEM and found a linear relationship between strain and $1/r$ (Figure 4-1), with a slope yielding a value of the surface stress of 1.2 J/m^2 . For an arbitrary microstructure, Weissmuller and Cahn [64] derived the general expression:

$$3V\langle\Delta P\rangle_V = 2S\langle f\rangle_S \quad (3)$$

which relates the mean pressure in a solid to the interface stress where $\Delta P = P - P_{ext}$, V is the volume, S is the total surface area, and $\langle f\rangle_S$ is the mean surface stress.

Combination with Hooke's law (Equation 1) results in

$$\langle f\rangle_S = \frac{-9K\varepsilon_a V}{2 S}. \quad (4)$$

Swaminarayan et al. [68], used the EAM with the potentials of Foiles [69] to quantify surface properties of spherical crystallites of fcc metals with radii, r , in the range of $3a_0 < r < 14a_0$ where a_0 is the lattice constant. They calculated the surface energy and surface stress as well as the lattice parameter and mean pressure in the center of the spheres.

Both the lattice parameter and pressure were found to be directly proportional to the inverse sphere radius as predicted by the Laplace-Young equation. They calculated the surface stress of gold to be approximately 1.1 J/m^2 in agreement with the experimental data of Mays.

As a baseline for our potentials, a series of simulations for the relaxation of spheres similar to that described above were performed. The spherical structures for the simulation were generated by first creating a large cube of an fcc lattice centered on a tetrahedral site and then removing all atoms whose distance from the center was greater

than the desired radius, r , with r in the range of 20 to 100Å. The spheres were then relaxed at zero K using a molecular statics energy minimization process using a standard conjugate gradient technique with both the Johnson and Trimble potentials. The convergence criterion was such that the maximum force on any given atom was less than 1×10^{-4} eV/Å. The average strain was then calculated from the lattice parameter in the center of the relaxed spheres as, $\varepsilon_a = \frac{a_f - a_i}{a_i}$, to give us a direct comparison to the experimental values. The value of the lattice parameter in the center of the spheres was calculated as follows. The average nearest distance was calculated for each individual atom. The average nearest neighbor distance for the atoms nearest the center of the spherical particle was then calculated. This value was then multiplied by $\sqrt{2}$ in order to obtain the lattice parameter, a_f . The results of the simulations with both potentials are plotted together with the experimental data of Mays [70] in Figure 4-1.

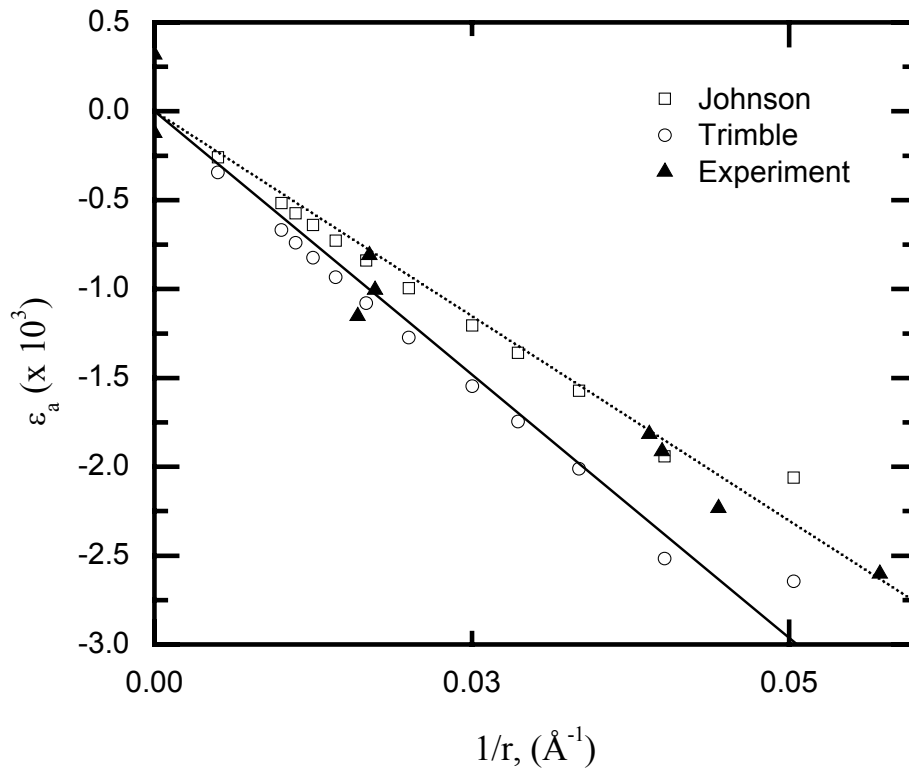


Figure 4-1 – Plot of strain vs. $(1/r)$, where r is the initial unrelaxed radius, observed for spherical particles from the experimental data of Mays (\blacktriangle) and for EAM simulations using the Johnson (\square) and Trimble (\circ) potentials.

The strain predicted by the simulations (ϵ_a) is in good agreement with the experimental data of Mays [70]. The surface stress for both potentials was calculated by performing a linear fit to the data of strain vs. $1/r$ shown in Figure 4-1 and using Equation 2. The Johnson potential gives $f = 1.15 \text{ J/m}^2$ and the Trimble potential gives $f = 1.47 \text{ J/m}^2$. An interesting point to note is that the original Johnson potential more closely fits the experimental data for surface stress than the Trimble potential that was modified to more accurately reproduce surface properties (i.e. stabilize the (111) surface reconstruction).

We now consider the overall change in sphere size as referenced to the completely unrelaxed state, i.e. the initially generated structure of radius, r . The actual change in sphere radius consists not only of the curvature dependent strain, ε_a , as given in Equation 2 but also any additional surface relaxation, d_{surf} , i.e. the total sphere relaxation, $\frac{\Delta r}{r}$, is given by

$$\frac{\Delta r}{r} = -\left(\frac{2f}{3K} + d_{surf}\right)\frac{1}{r} \quad (5)$$

The magnitude of the term, d_{surf} , is significant as shown in Figure 4-2. Fitting the simulation data in Figure 4-2 to Equation 5 gives values of $d_{surf} = 0.27$ and 0.33\AA as compared to $\frac{2f}{3K} = 0.046$ and 0.059\AA for the Johnson and Trimble potentials respectively. The significance of this finding can be appreciated when examining the macroscopic relaxation of bicontinuous microstructures which we show is also dominated by the surface relaxation term (d_{surf}).

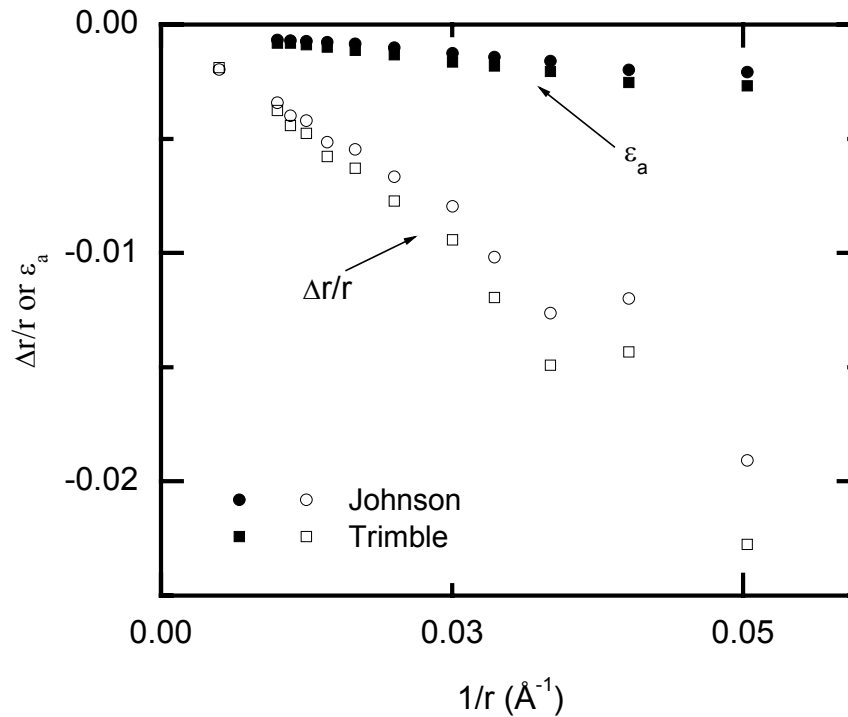


Figure 4-2– Simulation results of overall spherical cluster relaxation, $\Delta r/r$ as compared to that expected for a mean pressure induced relaxation only, ϵ_a . Both the Johnson and Trimble potentials are shown.

Surface relaxations have been experimentally measured [71] as well as simulated by numerous techniques for single crystal faces. The magnitude of the surface relaxations depend on many factors including surface orientation and the presence of any surface reconstructions. Surface relaxations have been observed to be both inward and outward depending upon the experimental conditions (i.e. surface environment). In the case of a pure element, EAM potentials always predict inward surface relaxations.

In order to generate representative bicontinuous structures with periodic boundary conditions amenable to EAM simulations, a phase-field model simulating the spinodal decomposition of a binary alloy was used. It has been shown that the morphology of dealloyed Au is quantitatively similar to the morphology of spinodally decomposed systems as determined by small angle neutron scattering (see for example [72]). For the phase-field model[73], the evolution of the spinodal microstructure was described by the Cahn-Hilliard equation, $\frac{\partial c}{\partial t} = -\nabla^2 (F(c) + \nabla^2 c)$, where c is the local composition and F is the local free energy density function[74]. In our case F is a simple double well potential. Since this equation is non-linear it was solved numerically through discretization in space and time. The structure that results from the simulation is two-phase and bicontinuous. One of the phases is then removed and interpreted as the pore space while the remaining phase is interpreted as gold. The pore volume fraction of all samples in this study was 0.5. During the phase-field simulation, structures at several time steps were acquired, thereby creating structures with varying ligament/pore sizes. Chord length measurements were used to characterize the pore and ligament widths. A representative structure generated by the phase-field method is shown in Figure 4-3 along with a microstructure calculated using the Berk model [75] and based on small angle neutron scattering data taken for porous gold [76].

The Berk model is based upon an algorithm proposed by Cahn[77] for simulating spinodally decomposed morphologies in two-phase systems where a well defined length scale emerges. Cahn's construction associates an interface between two phases with a

contour of a random standing wave, $S(\vec{r})$, composed of N wave vectors chosen random in amplitude, A_n , direction, \hat{k}_n , and phase, ϕ_n , but having a narrow distribution in length, $k = 2\pi/\lambda$.

$$S(\vec{r}) = \frac{1}{(N\langle A^2 \rangle)^{0.5}} \sum_{n=1}^N A_n \text{Cos}[k\hat{k}_n \cdot \vec{r} + \phi_n]$$

A two phase morphology is created by choosing a contour of this set $S(\vec{r}) = \alpha$ and assigning all points for which $S(\vec{r}) > \alpha$ to phase 1 (metal) and all points for which $S(\vec{r}) < \alpha$ to phase 2 (pore). The bulk fraction of the metal phase is given by $f_m = (1 - \text{Erf}[\alpha]) / 2$. The special case of an isometric partition where the phase fractions are equal corresponds to the contour, $S(\vec{r}) = 0$. Berk showed that the scattering from such a geometric construction displays a sharp diffraction peak at $k = 2\pi/\lambda$. By allowing for dispersion in k , one can fit the broader scattering peaks observed in experimental data. The dispersion can be defined by any appropriate distribution function. We have found that typically the log-normal function or the Schultz distribution best fits the experimental data for np-Au. More detail on the Berk model can be found in Chapter 5.

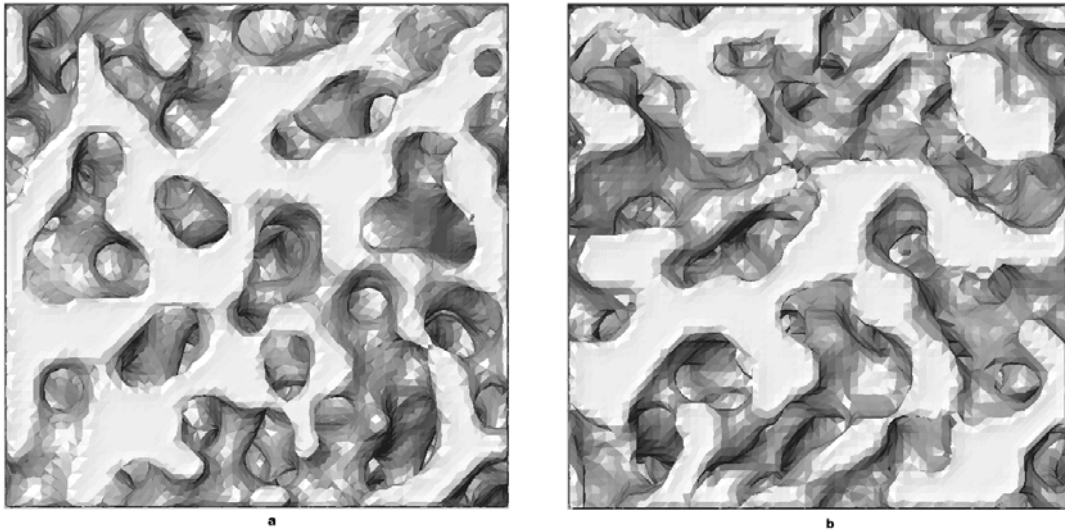


Figure 4-3 – Surface images of structures generated with the a) phase field model and the b) Berk model.

In order to analyze the surface stress effects in these np-samples, we utilize the general expression derived by Weissmuller and Cahn [32] given in Equation (3). The surface area, S , in this equation is determined directly from the simulations through a calibration procedure utilizing spherical clusters.

The surface atoms (A), those with coordination < 12 , were counted for a series of spherical solids as well as spherical holes of the same set of radii. This provides a set of structures with zero mean curvature and a known surface area, $4\pi r^2$. This calibration was determined for unrelaxed surfaces. The linear behavior between S and A shown in Figure 4-4 allows us to find the calibration factor (slope) over the same value of zero mean curvature and length scales observed in the np-structures. A measure of the surface area for a given np-structure is then determined by counting the surface atoms and multiplying by the calibration factor. This method allows us to get an estimate of the

surface area of the nanoporous structures. A possible drawback of using this method is that the surface area is largely independent of strain.

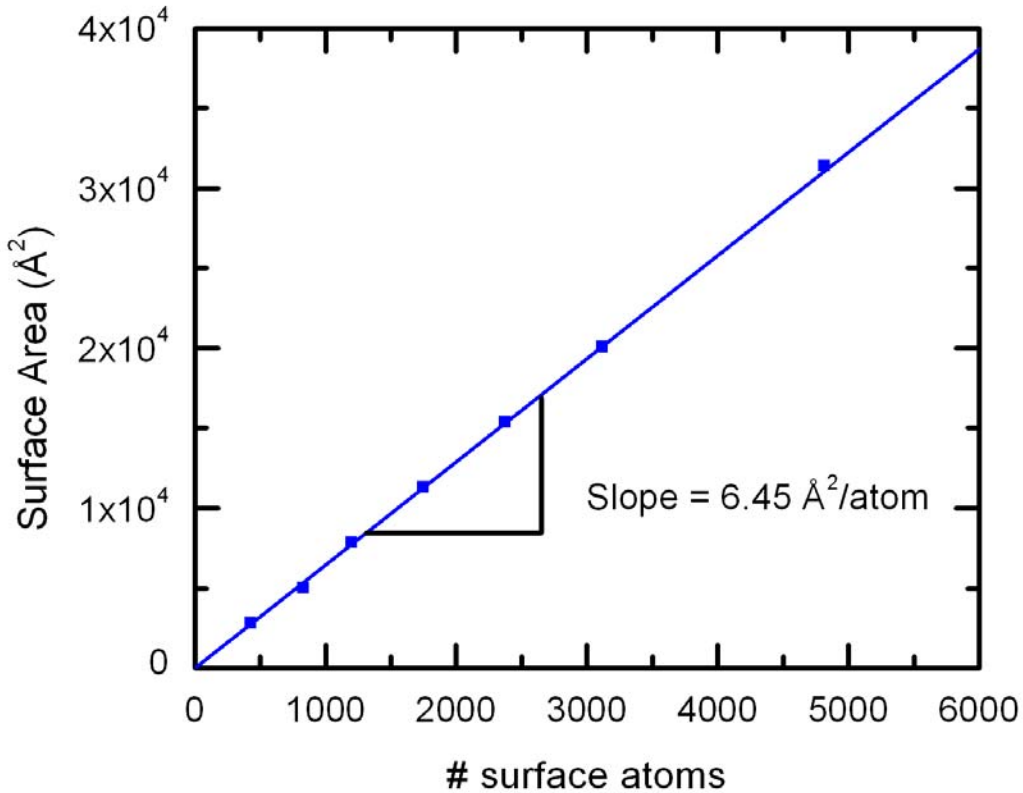


Figure 4-4 – Surface area calibration plot based on the number of surface atoms of unrelaxed spherical particles and spherical voids with known surface areas.

After initial generation, the samples were relaxed with molecular statics allowing for an additional isotropic relaxation of the total volume of the sample. This procedure results in relaxed np-structures in which the strain induced by the free surfaces can be determined.

This relaxation in terms of the change in cube edge length, $\Delta L/L$, is shown in Figure 4-5 along with the previous results for total sphere relaxation, $\Delta r/r$, now plotted versus

S/V rather than $1/r$. Also plotted in Figure 4 is the mean strain measured at the center of the metal ligaments within the relaxed np-structure. This mean strain is consistent with the generalized capillary equation (Equation 4) and gives the expected value of the surface stress as determined by the spherical relaxation data. However, as shown the total macroscopic relaxation is much greater than that given by the mean pressure. In fact, the macroscopic relaxation is also dominated by the surface relaxation term and is consistent with total spherical relaxation data, $\Delta r/r$.

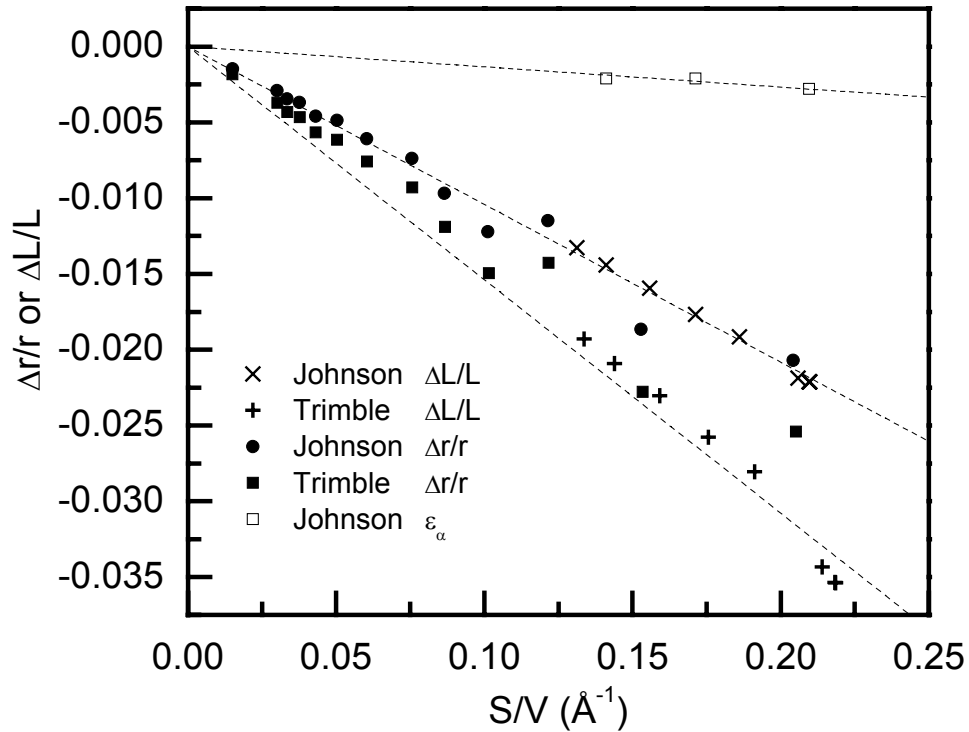


Figure 4-5 – Relaxation of nanoporous (NP) Au $\Delta L/L$ compared to that of the spherical clusters $\Delta r/r$ for both the Johnson and Trimble potentials. Also, plotted is the strain, ϵ_a , in the center of the np-Au metal ligaments for the Johnson potential. The average ligament diameters for the nanoporous structures range from 12.8 to 17.6 \AA .

We can write an analogous equation to that of Equation 6 for the np-structures as:

$$\frac{\Delta L}{L} = - \left(\frac{2\langle f \rangle_s}{9K} + d_{surf} \right) \frac{S}{V} \quad (6)$$

where d_{surf} is found to be identical to that given by the spherical relaxation data. For the spherical clusters S/V corresponds to the length scale $3/r$. However, for np-metals the S/V ratio must be measured directly since it depends upon a minimum of 2 independent parameters for a given volume fraction of porosity [78], i.e. S/V is not simply proportional to an average length scale such as the ligament diameter.

Kramer et al, have recently demonstrated the surface-stress induced actuation capability of np-gold formed by dealloying. Linear strains on the order of 1×10^{-4} in gold (1.2x1.2x1 mm) with a potential variation of approximately 0.65 V [14] were observed. Typical values of the change in surface stress with potential for polycrystalline gold have been measured at 1 J/m²/V [66] indicating a change in f of 0.65 J/m² in this case. These samples had a pore fraction of 0.75 and ligament widths of approximately 20 nm. An estimate of the surface area to volume ratio of $8.5 \times 10^{-4} \text{ \AA}^2 / \text{ \AA}^3$ was made using the Berk model with typical values for dispersity in pore sizes observed experimentally in dealloyed metals [31].

We now present a simplified calculation to compare our simulation results to these experimental data. The results of the two potentials will be used to estimate the strain resulting from a change in f from 1.15-1.47 J/m² ($\Delta f = 0.32$) for the Johnson and Trimble potentials respectively. Extrapolation of the simulation results to the estimated

S/V ratios of the experimental samples predicts a strain of 2×10^{-5} for a $\Delta f = 0.32$ or approximately 4×10^{-5} for $\Delta f = 0.65$ which is in reasonable agreement with the experimental results of 1×10^{-4} . We note that if one neglects the surface relaxation term a strain of only 1×10^{-5} would be predicted.

In conclusion, the geometric volume change of np-structures has been shown to be significantly dependent upon surface relaxation in addition to the curvature dependent mean pressure given by the generalized capillary equation. We show that this is a reasonable expectation for spherical particles and np-solids based on the magnitude of the surface relaxation term and agrees with the observed actuation measurements in the literature.

Acknowledgements

S.G. Corcoran and D.A. Crowson acknowledge support for this work by the National Science Foundation under Grant No. DMR – 0301007. D. Farkas acknowledges support from NSF, Materials Theory Program. The authors acknowledge use of the Virginia Tech System X Terascale Computing Facility.

4.2 Supplemental Material

This section contains supplementary materials describing in additional detail the simulations and results contained in the above paper (4.1).

4.2.1 Bi-continuous Structures

The structures generated with the phase-field model are shown below. The pictures are surface view images created by Amira 3.0 (a commercial 3D data visualization software package). The surfaces are found using the point wrap algorithm. This algorithm performs a surface reconstruction from a set of unorganized data points. It models a probe sphere that is dropped onto and rolled over the set of data points. Every three points the sphere rests on becomes a triangle in the resulting surface.

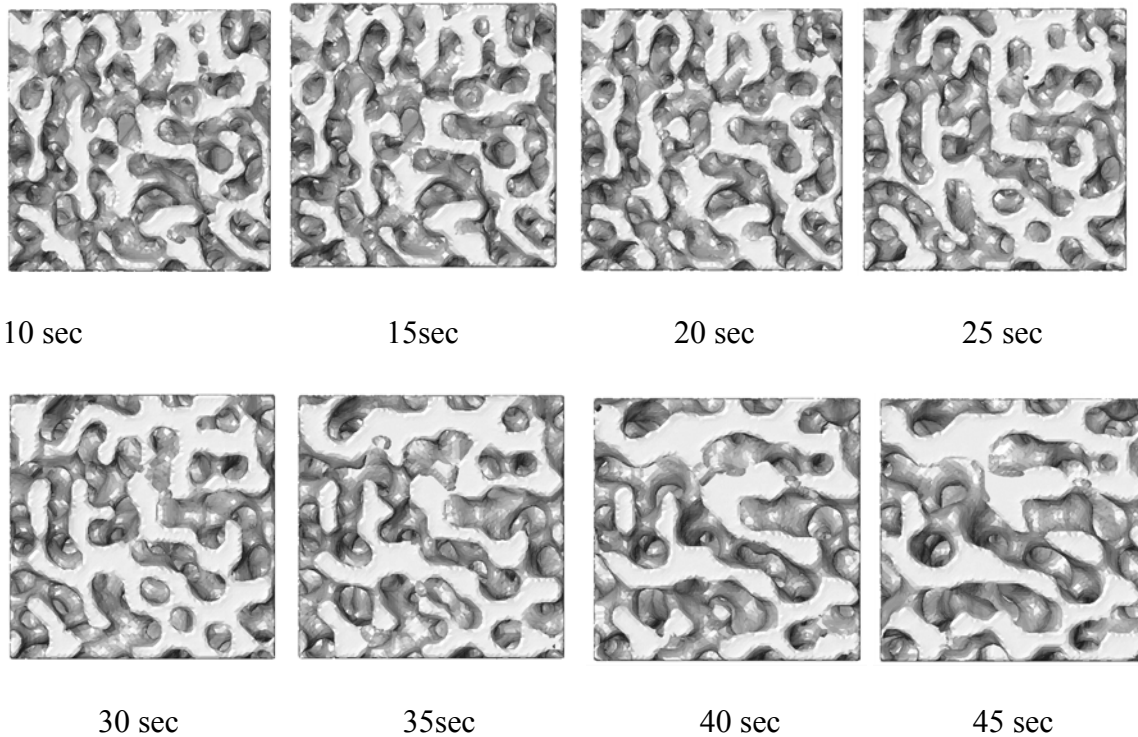


Figure 4-6 -- Surface images of the bicontinuous structures used in the simulations shown above.

The average ligament diameters for the structures were calculated by measuring chord length distributions of the 3D structures. The average ligament diameter was extracted by fitting a log-normal distribution to the chord length measurements. The results of these calculations are listed in Table 4-1.

Table 4-1 – Average ligament diameters for porous structures calculated with chord lengths.

	10	15	20	25	30	35	40	45
Average ligament diameter $v_f=0.5$	12.8	12.8	12.9	13.9	14.5	15.5	16.6	17.6
Average ligament diameter $v_f=0.7$	10.5	10.7	10.5	10.7	11.0	11.6	12.2	13.4

4.2.2 Spherical Voids

To further validate our results for the overall geometric relaxation of the nanoporous metals, a series of cubes of varying edge length were created, each with a spherical void in the center. This yields structures with periodic boundaries and a simple geometry in which the surface area and volume can be easily calculated. According to the generalized capillary equation,

$$3V\langle\Delta P\rangle_V = 2S\langle f\rangle_S,$$

the relaxation of these void structures should be the same as that of a sphere with the same surface area to volume ratio. This is of course under the assumption that the average surface stress is the same for spherically concave and convex surfaces. The

results for the overall relaxation of the void structures with the Johnson potential, $\Delta L/L$, are plotted together with the results for the spheres, $\Delta r/r$ in Figure 4-6.

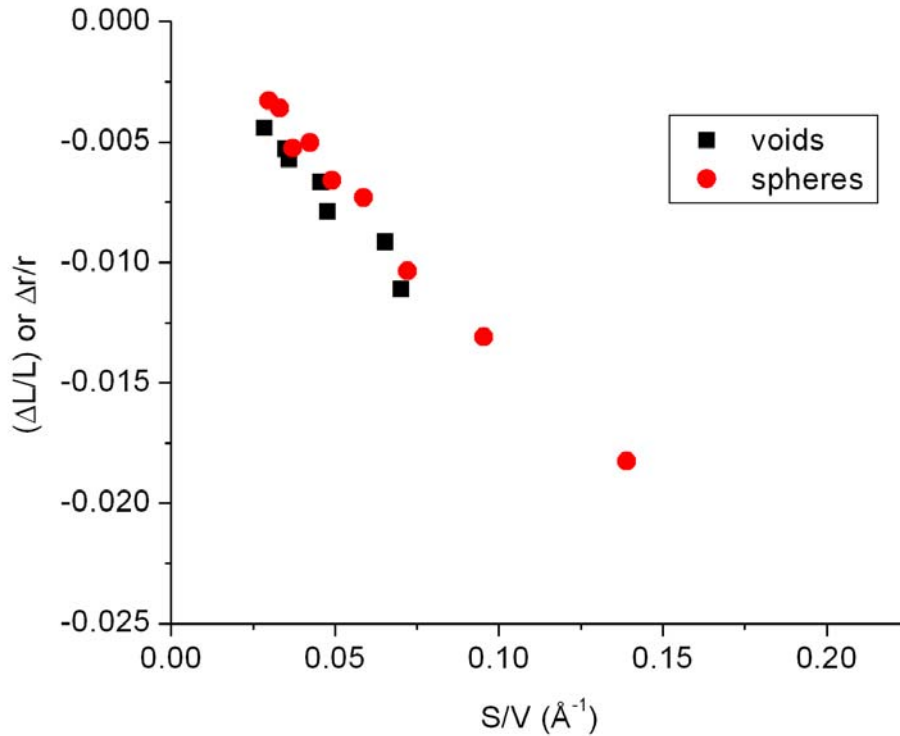


Figure 4-7 -- Shown here is the strain in spherical clusters as well as strain in periodic cubes with spherical voids versus surface area to volume ratio.

There is a very good agreement between the two data sets indicating that the surface relaxation makes a very significant contribution to the overall geometric relaxation of these structures as is observed with the nanoporous structures. The slight differences in the data for the spheres and the voids could possibly be due to the average surface stress being slightly different for concave as opposed to convex surfaces. These simulations were performed using molecular statics as in the case of the nanoporous structures.

4.2.3 Sphere Radius Definition

The definition of the radius of a spherical cluster of atoms can be somewhat ambiguous. In this case we have a discrete set of atom coordinates and not a continuum sphere. The radius for this set of atoms needs to be defined in some way. In all of the results shown above, the radius was defined as the furthest distance of any atom in the set from the center of the particle. This can be thought of as an upper bound for the value of the radius. Another method would require the definition of a surface layer. Then the radius could be determined by calculating the average distance of the atoms within this layer to the center of the sphere as the radius. The surface layer could be determined by selecting all atoms with a coordination number less than some threshold number. The radius determined by this method would necessarily decrease with an increase in the thickness of the surface layer. Figure 4-7 shows the different results for $\Delta r / r$ calculation with the maximum r and also by defining atoms having <10 nearest neighbors as surface layer atoms. The results show that $\frac{\Delta r}{r}$ is significantly affected by the precise definition of r .

The best method for determining r is open to debate.

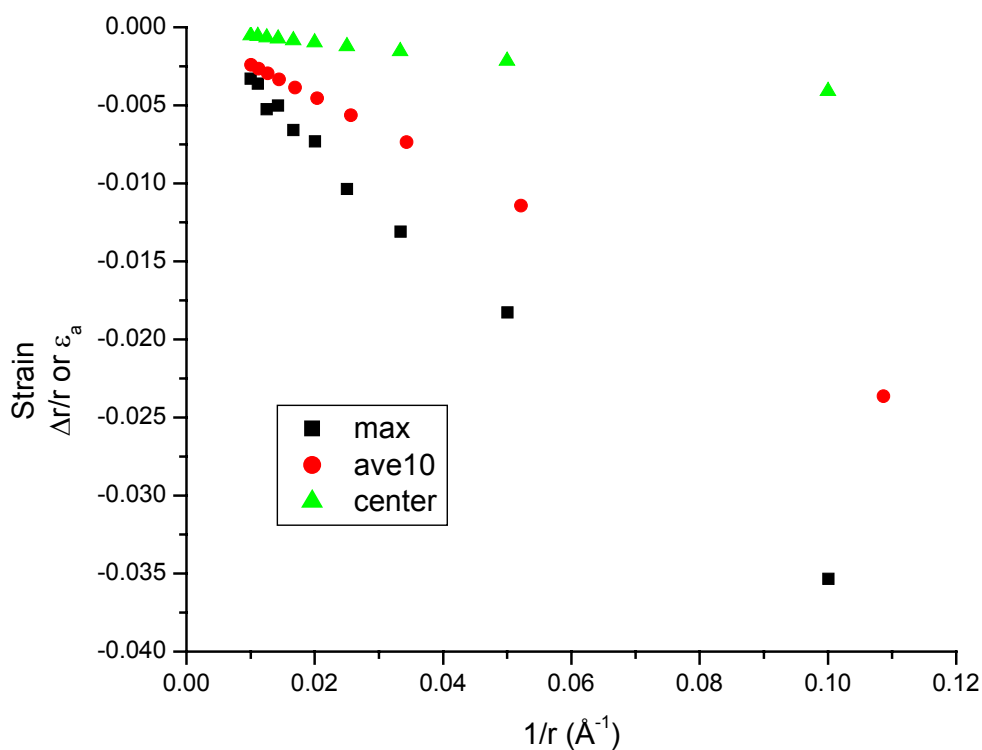


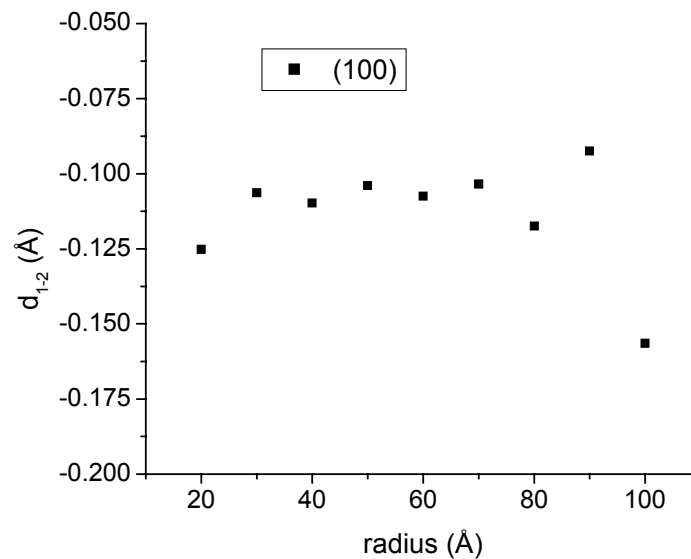
Figure 4-8 – Strain in spherical particles relaxed with MS and the Johnson potential calculated in two ways with two different definitions of the radius.

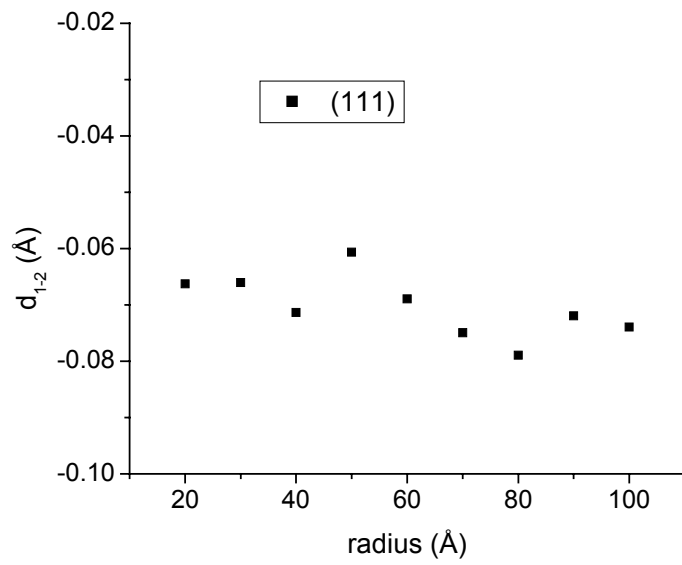
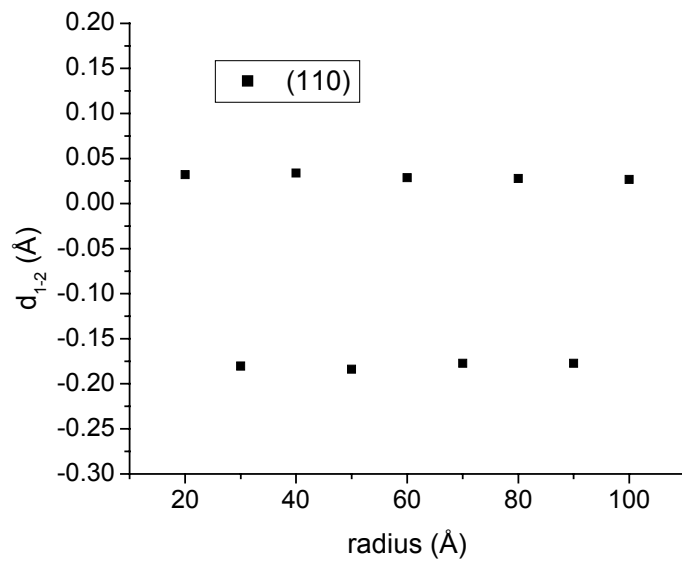
4.2.4 Directional Surface Relaxations

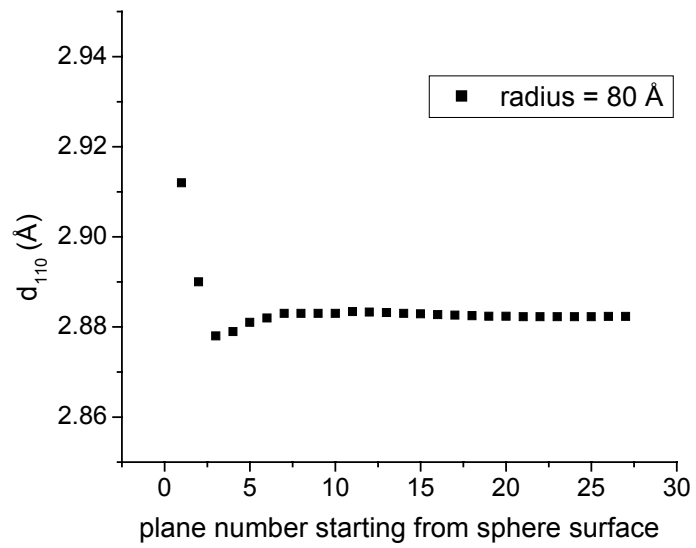
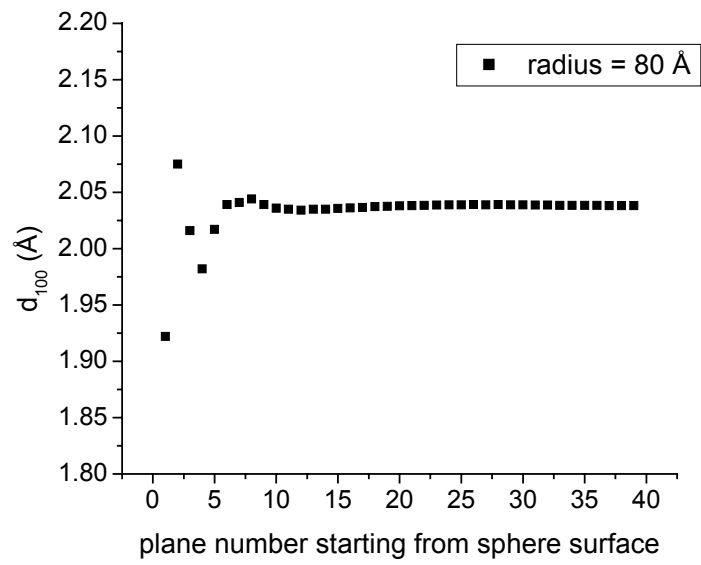
Directional multilayer surface relaxations were calculated for the spherical clusters relaxed with the Johnson potential. The first 3 plots in Figure 4.9 are relaxation of the first atomic planes in the (100), (110) and (111) directions plotted as a function of the radius. d_{1-2} is calculated as the difference between the perfect single crystal plane spacing in the direction of interest and the relaxed plane spacing of the first atomic layer. The plots show that there is an inward relaxation of the first atomic layer in the (100) and

(111) directions however in the case of the (110) direction the can be either an inward relaxation or a slight outward relaxation depending upon the value of the radius.

The following 3 plots are of the plane spacings vs the plane number starting from the sphere surface for an 80Å sphere relaxed with the Johnson potential. These plots are for the 3 directions (100), (110) and (111). For the (100) and (111) directions, there is a large compressive strain of the first atomic layer followed by a smaller tensile strain in the second layer. The strains oscillate somewhat as until a stable value is achieved near the center of the particle. In the (110) direction there is a small tensile strain of the first two atomic planes and then a stable value of the strain is achieved.







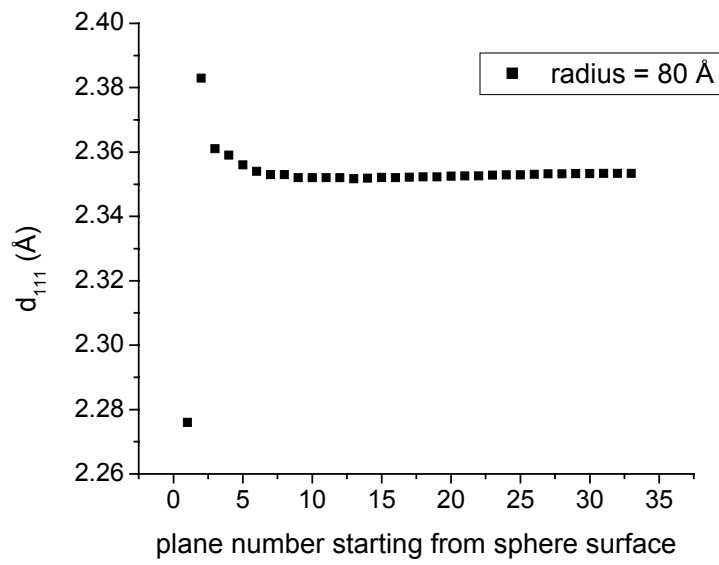


Figure 4-9 – Multilayer relaxation in spherical particles relaxed with the Johnson potential in the three directions (100), (110) and (111).

4.2.5 Mean Pressure in Ligaments

The mean pressure in the center of the ligaments was calculated by plotting a histogram of the number of atoms with a nearest neighbor distance within in a given bin.

Histograms for one of the structures are shown in Figure 4.10 below to illustrate the method. The largest peak occurs at the highest value of the nearest neighbor distance.

This corresponds with the lowest value of strain which occurs in the center of the ligaments whereas the peaks at lower nearest neighbor distances correspond to atoms in higher states of local strain at the surfaces. The local strain of a surface atom will be

dependent upon its local environment. The atom could be on a surface facet, a step edge, the atom could be an adatom on the surface, the strain determined in this way will also be dependent on the specific orientation of the surface. The mean pressure was determined from the strain at the largest peak in the histogram by simply multiplying the strain by the bulk modulus.

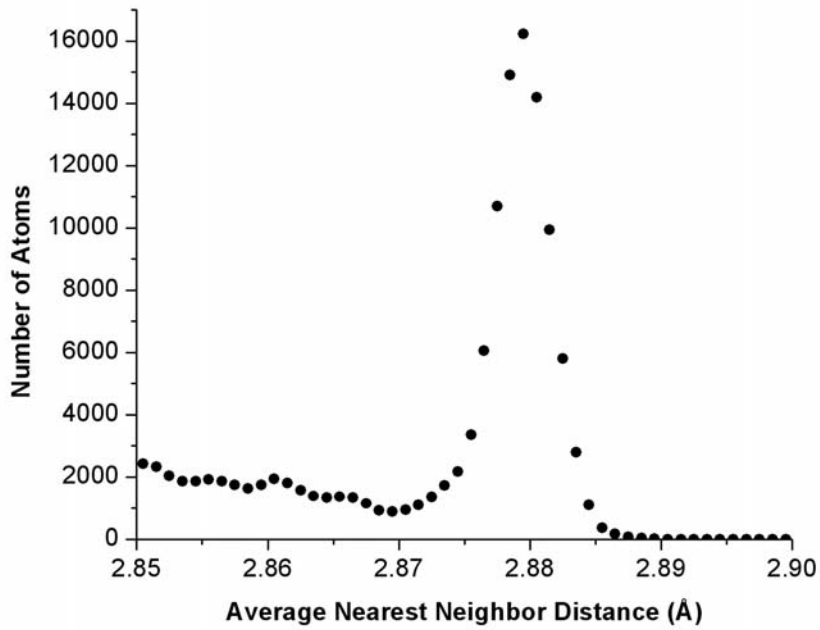
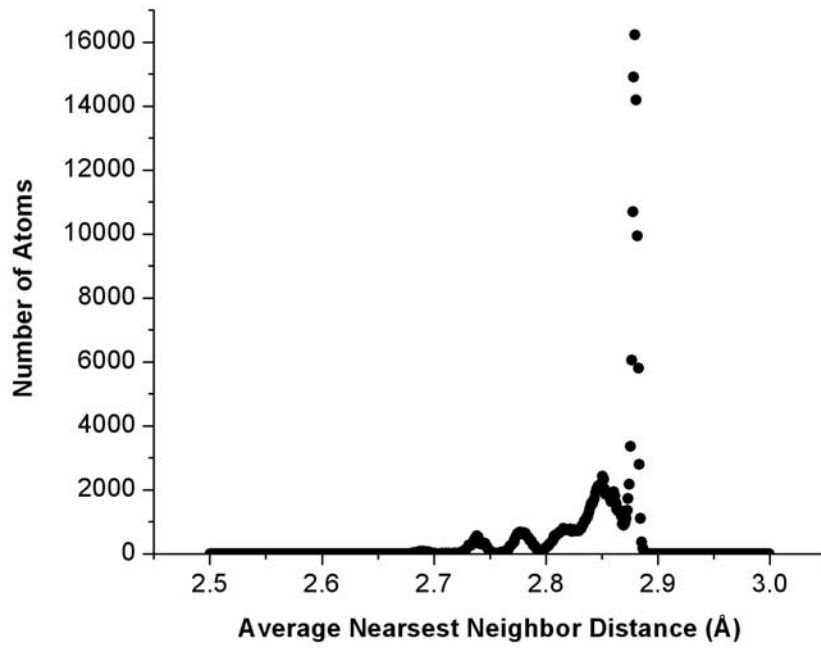


Figure 4-10 – Histogram of the number of number of atoms with a given value of the average nearest neighbor distance. This corresponds to the average local strain around a given atom.

CHAPTER 5 Capillary Driven Mechanical Instability of Nanoporous Metals: Bridging Length Scales between Experiment and Atomistic Simulation

This Chapter is written in the form of a paper that was submitted to Nature of Materials (5.1) along with some pertinent supplemental information (5.2).

5.1 Capillary Driven Mechanical Instability of Nanoporous Metals: Bridging Length Scales between Experiment and Atomistic Simulation

5.1.1 Abstract

We present a method for generating model bicontinuous metal / void structures for use in atomistic simulations of bicontinuous nanoporous solids. The structures are generated with periodic boundary conditions using a phase-field model to simulate the spinodal decomposition of an ideal system. One phase in the model is then associated with the pore volume while the other phase is associated with the metal ligaments. Small angle neutron scattering was used to quantitatively compare experimental samples to that generated by the phase field method. EAM results using model structures with experimentally accessible length scales are presented which demonstrate the potential of such simulations in understanding the behavior of nanoporous metals. The simulation results presented identify a maximum surface area to volume ratio necessary to maintain mechanical stability beyond which the pore structure collapses.

5.1.2 Letter

The corrosion process known as dealloying [9] has promise as a method to create nanoporous metals and in fact found use thousands of years ago by the incas of pre-columbian South America as a method of depletion gilding[1]. A dilute gold alloy was immersed in a corrosive bath where the less noble element of the alloy, typically copper, was slowly removed leaving behind a pure gold “sponge-like” layer at the surface. This porous layer was then consolidated by burnishing.

Figure 5-1 shows a representative micrograph of porous gold. The as-prepared ligament diameter can be as small as 3 nm.

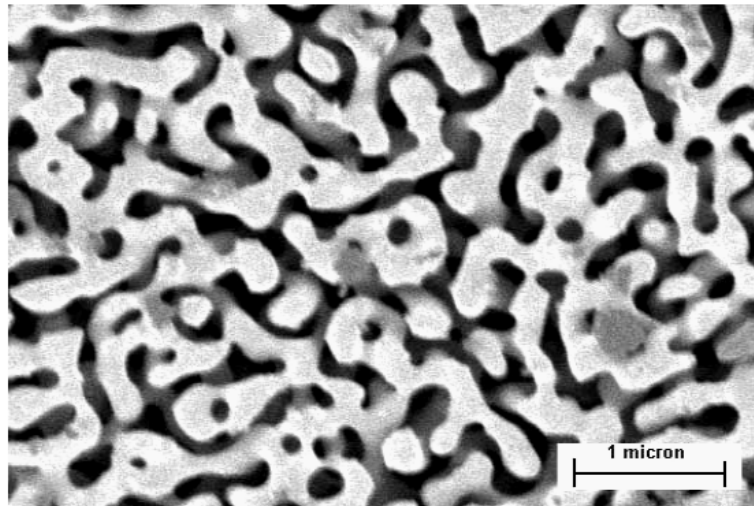


Figure 5-1 -- Porous gold created by the selective dissolution of Ag from a $\text{Ag}_{0.7}\text{-Au}_{0.3}$ alloy in concentrated nitric acid. The sample was coarsened by a post dealloying heat treatment. The as-prepared ligament diameter can be as small as 3 nm.

An understanding of the dealloying process, and its technological importance, has advanced significantly over the past few decades. Calvert and Johnson in 1866 were the

first to make mention of this process in the scientific literature[17]. Eventually, a link between dealloying and the seasonal cracking of brass alloys was identified with the brittle nature of these porous structures[18, 19]. The electrochemical aspects of the dealloying process, polarization curve behavior, critical potential measurement as well as the details of morphology development have been studied by numerous researchers[10, 21, 27, 72, 79-83]. Recently a broad range of applications for these structures have been identified including catalysts for fuel cells[84], specialized filtration, biological sensors[85], skeletal structures for fundamental studies [61] and electrochemical actuators[13].

The actuation properties of the structures are a result of the fact that in electrochemical systems, the surface stress (and hence capillary pressure) can be varied through the application of an electrochemical potential. The isotropic surface stress, f , is given by

$$f = \gamma + \frac{\partial \gamma}{\partial \varepsilon}$$

where γ is the isotropic surface free energy and ε is the elastic strain. This

effect was experimentally explored by Lin and Beck[30] by measuring the extension of long thin polycrystalline gold ribbons as a function of the applied electrochemical potential. This effect has been recently exploited in nanoporous gold (np-Au) to produce surface stress induced reversible strain amplitudes comparable to commercial piezoelectric materials [86].

The main focus in the letter is to use atomistic simulations to explore the stability of nanoporous metals to capillary stresses. Our unique contribution to this area is the ability to produce quantitatively representative structures with experimentally achievable length

scales as direct input into the atomistic models and hence bridging the length scales between experimental and theoretical studies in this area. Given that the average ligament size in a typical nanoporous metal sample is still on the order of a few nanometers, the generation of a model structure of sufficient size to avoid the effects of the non-periodic boundaries would typically make atomistic simulations infeasible. We have overcome this problem by using phase field modeling to generate quantitatively similar structures to those of experimental systems but with the added benefit of having periodic boundaries. The periodic boundaries allow for the simulation of smaller volumes of material that behave similarly to if they were infinite in extent.

Specifically, we (1) use small angle neutron scattering to determine average ligament sizes and their distributions in nanoporous gold created by dealloying and demonstrate the quantitative similarity between spinodal structures and bicontinuous nanoporous metals, (2) use phase field modeling to simulate the spinodal decomposition of a model system where the critical length scale in the system matches that of experimentally prepared samples, (3) take the resultant phase field structure and interpret one phase as Au and the second phase as void, and (4) use these final structures as direct input into molecular dynamic simulations using EAM potentials. The relaxation of the structures was measured as a function of the surface stress and ligament diameter. We show that the structures undergo a mechanical instability at a critical value of the mean capillary pressure which leads to an amorphization of the structure during pore collapse.

Figure 5-2, shows the *in situ* small angle neutron scattering (SANS) data taken during the dealloying of a $\text{Ag}_{0.70}\text{Au}_{0.30}$ foil in concentrated nitric acid. The formation of a scattering peak in these samples corresponds to the presence of a well defined length scale in the structure and was first explained by Berk[87] for the scattering of bicontinuous microemulsions. A fit to the scattering data allows for the generation of simulated structures (Figure 5-3). The average ligament diameter was found by making chord length measurements through these simulated images. The shifting peak position in Figure 5-2 corresponds to a coarsening of the average pore-ligament length scale. The average ligament size and coarsening behavior is a function of applied voltage, electrolyte composition[58], and coarsening potential. Ligament diameters as small as 3 nm were obtained in np-Au.

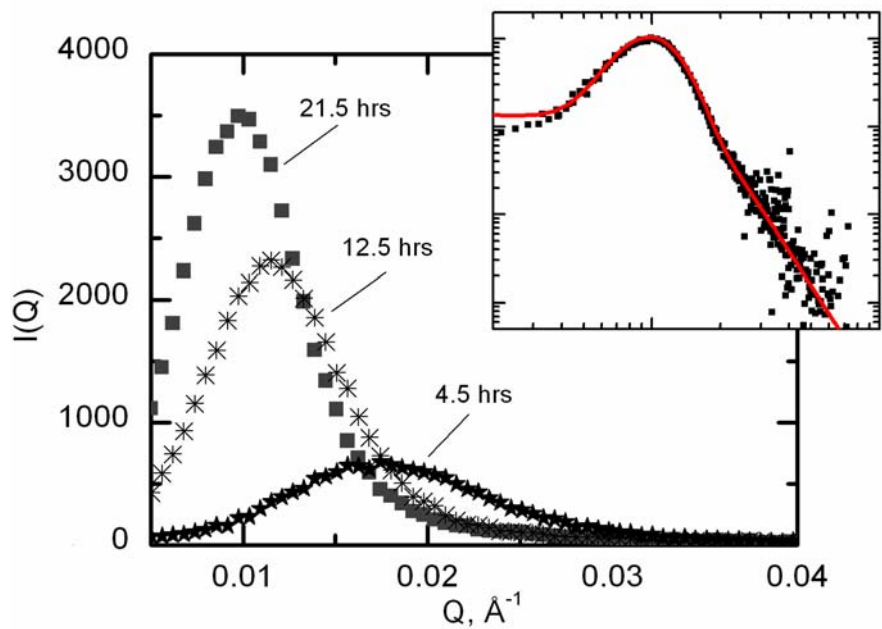


Figure 5-2 -- In Situ SANS data of dealloying. In Situ SANS data taken during the dealloying of $\text{Ag}_{0.7}\text{Au}_{0.3}$ in conc. Nitric Acid. Inset: Log-Log representation of Normalized SANS data showing the goodness of fit (red line) using the Berk model with the dispersion of wavevectors defined by the Schultz distribution ($z = 13$).

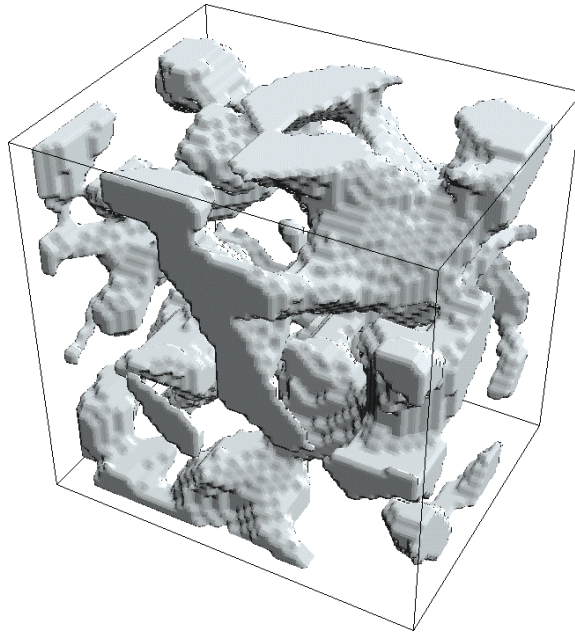


Figure 5-3 -- Simulated nanoporous gold. Simulated 3-d slice through a bicontinuous structure calculated using the Berk fit. The pixel resolution in the image above was on the order of an atomic Au radius.

There are several scattering models in the literature that have been applied to bicontinuous morphologies as observed for example in microemulsions and porous Vycor. Of these, the model given by Berk [78, 87] and that given by Teubner and Strey[88] were the first to reproduce the presence of the scattering peak observed in bicontinuous systems. The Berk model is based upon an algorithm proposed by Cahn[89] for simulating spinodally decomposed morphologies in two-phase systems where a well defined length scale emerges. Cahn's construction associates an interface between two phases with a contour of a random standing wave, $S(\vec{r})$, composed of N wave vectors chosen random in amplitude, A_n , direction, \hat{k}_n , and phase, ϕ_n , but having a narrow distribution in length, $k = 2\pi/\lambda$.

$$S(\vec{r}) = \frac{1}{(N\langle A^2 \rangle)^{0.5}} \sum_{n=1}^N A_n \text{Cos}[k\hat{k}_n \cdot \vec{r} + \phi_n] \quad (5-1)$$

A two phase morphology is created by choosing a contour of this set $S(\vec{r}) = \alpha$ and assigning all points for which $S(\vec{r}) > \alpha$ to phase 1 (metal) and all points for which $S(\vec{r}) < \alpha$ to phase 2 (pore). The bulk fraction of the metal phase is given by $f_m = (1 - \text{Erf}[\alpha]) / 2$. The special case of an isometric partition where the phase fractions are equal corresponds to the contour, $S(\vec{r}) = 0$. Berk showed that the scattering from such a geometric construction displays a sharp diffraction peak at $k = 2\pi/\lambda$. By allowing for dispersion in k , one can fit the broader scattering peaks observed in experimental data. The dispersion can be defined by any appropriate distribution function. We have found that typically the log-normal function or the Schultz distribution best fits the experimental data for np-Au.

The nice aspect of the Berk model is that after a fit is found to a set of experimental data equation (1) allows for the reconstruction of the scattering volume in real space. A three-dimensional slice through one of these structures is shown in Fig. 3. Given infinite computation power, large volumes of nanoporous metals could be simulated directly from the fits found in the Berk model. However, real limitations require unreasonably large samples to avoid edge effects from dominating the behavior of the simulation. For this reason, we chose to pursue the creation of model structures with quantitatively similar bicontinuous morphologies but with the added benefit of having the geometric condition of periodic boundaries. Given the ability to fit the scattering of np-Au by the

Berk model which is based on an algorithm developed to represent spinodally decomposed systems, we decided to explore the use of phase field modeling of an ideal spinodal system as a means to generate a model bicontinuous structure to be used as input into atomistic simulations. The phase field model has built in periodic boundary conditions.

The model involves solving of the Cahn-Hilliard equation,

$$\frac{\partial c}{\partial t} = -\nabla^2 (F(c) + \nabla^2 c),$$

through numerical integration. In this equation, c is the local concentration and F is the local free energy density function. In our case we use a simple double well potential function given by $F(c) = 16(c^3 - 2c^2 + c)$. A simple finite difference method on a square lattice is used to perform the integration. The structures created by this model are two-phase and bicontinuous and have periodic boundary conditions as a result of the numerical integration algorithm. The spinodal structure evolves in time in this model through phase separation and coarsening of the two phase structure. We then interpret one of the two phases as the pure metal and the other phase is then removed in order to create the pore space. Bicontinuous structures of varying length scales can then be created by taking snapshots in time during the structural evolution. We characterize the size scales of these structures by extracting chord length distributions from the 3 dimensional data sets. The ligament size distributions are found to be comparable to those of structures created directly by the Berk model for the scattering of np-Au (*see supplementary Fig. 1*).

The model structures are then interpolated and resampled to an FCC lattice before use in the atomistic simulations. The embedded atom method (EAM) potentials of Haftel[90] were used for this study. This set of potentials was selected because they were designed to systematically vary the unrelaxed surface stress thereby allowing us to probe surface stress effects on the stability of nanoporous structures. The variation in surface stress of the potentials was achieved by progressively steepening the embedding function at electron density values typical of free surfaces (70-80% of bulk values). The potentials Au1-Au5 were generated from an initial potential, Au0, using this approach. The unrelaxed surface stress (f) was varied from 2.22-4.85 J/m^2 on the (100) surface which corresponded to a 2.28-7.32 J/m^2 for (111) surface.

The potentials were calibrated by performing energy minimizations of spherical particles of varying radius, r , using a standard conjugate gradient technique. A plot of radial strain vs. $1/r$ was linear and the slope was proportional to the surface stress as given by

$$\varepsilon = -\frac{2f}{3K} \frac{1}{r},$$

where K is the bulk modulus. The results of these simulations are shown in

column 4 of Table 5-1.

	(100)	(111)	f
Au 0			1.7034
Au 1	2.220	2.282	2.2134
Au 2	2.891	3.786	2.5245
Au 3	3.246	4.514	2.56785
Au 4	4.063	6.282	2.37915
Au 5	4.850	7.316	1.52745

Table 5-1 -- Surface stress given by EAM potentials of Haftel, et al. Columns 2 & 3 give the values of the surface stress on the (100) and (111) surfaces taken from ref. 26 while column 4 gives the results of the isotropic surface stress for relaxed spheres.

An interesting outcome of these calibration simulations is that as the surface stress of the potential is increased by steepening the embedding function the (100) and (111) surface reconstructions become stable. When this occurs, the surface atoms of the spherical particles are driven to rearrange in order to minimize the energy. This in turn reduces the pressure in the spherical particle and thus results in a lower value of the spherically averaged relaxed surface stress.

Nanoporous Au structures with average ligament diameters of 1.3, 1.4, 1.5, 1.8, 2.1, 2.7 and 3.6 nm were created using the phase-field model. A slice through one such structure is shown in Fig. 5-4 inset. The pore volume fraction for all of these structures was 0.5. Molecular dynamics (MD) equilibrations were then used to investigate the surface stress induced strains in these structures. The MD code LAMMPS was used for these simulations on System X at the Terascale Computing Facility of Virginia Tech.

The samples were relaxed using an isothermal-isobaric ensemble (NPT) at 1 K and 0 mean pressure. The relaxations were performed in the following manner for each of the 7 samples. The sample was first relaxed using potential Au0 (lowest f) until a stable value of the volumetric strain was achieved. The resulting structure was then relaxed with potential Au1 (increased f). This process of increasing the surface stress was continued until either all 6 potentials were used or until a volumetric strain greater than 20% was achieved indicating an instability of the porous structure. This series for the 1.8 nm ligament sample is shown in Fig. 5-4.

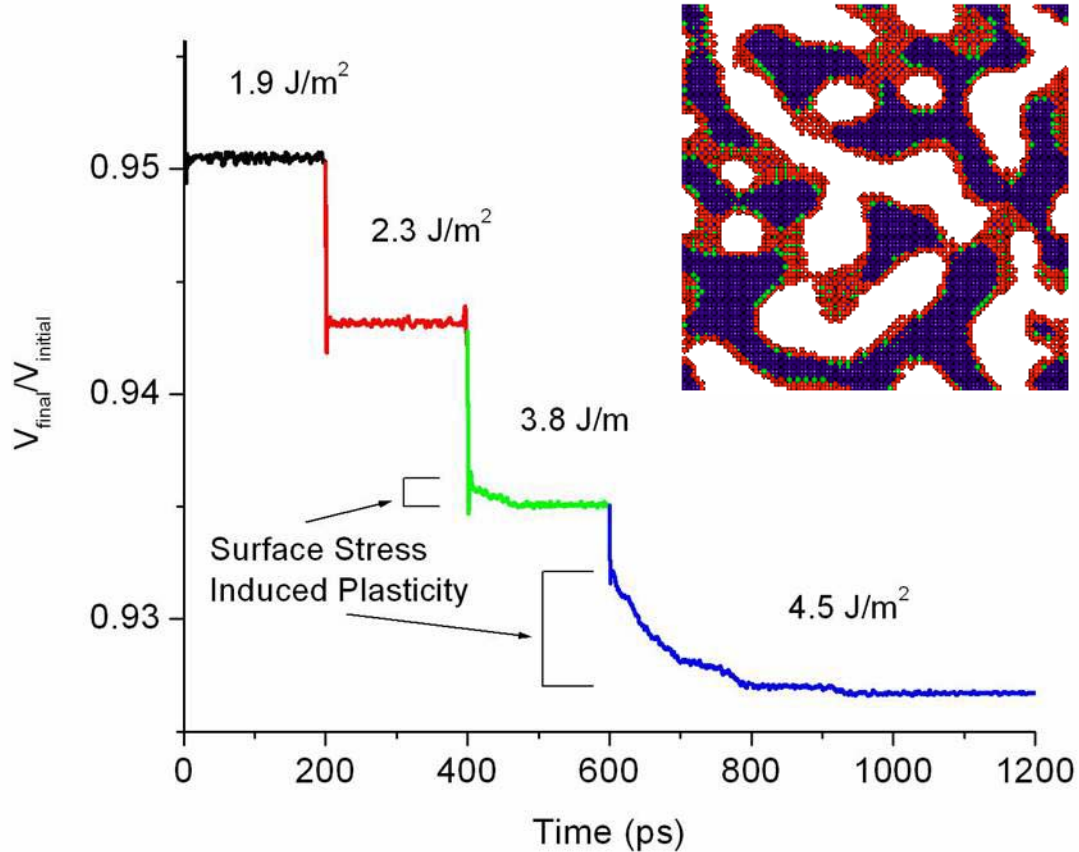


Figure 5-4 -- Relaxation curves for nanoporous gold. Volumetric strain for the 1.8 nm ligament sample after application of potentials Au1, Au2, Au3, and Au4 respectively. The value of the (111) unrelaxed surface stress is indicated on the figure for reference. The inset is a slice through the initial structure.

For the particular case of the 1.8 nm ligament sample, the potentials Au0 and Au1 show completely elastic compression of the structure. The relaxation curves shows an initial rapid jump in the volumetric strain; following this jump the volumetric strain remains stable. No dislocations or stacking faults were observed in the structure. With potential Au2 we see the first evidence of permanent deformation. The relaxation curve in this case shows a period of relatively slow increasing volumetric strain before a stable value

is reached. This is indicative of a plastic deformation process as indeed we can see in the stacking faults that appear in the atomic structures (*see supplementary figure 2*), where the atoms are colored by the centro-symmetry parameter[91].

A cycling of the potential back to Au1 and then returning to Au2 shows a recovery of only the elastic portion of the strain and now the potential can be cycled between Au1 and Au2 with completely reversible strain amplitude. The relaxation with potential Au3 indicates a larger amount of plastic deformation. This is evidenced by an increased stacking fault density observed in the images. Upon cycling, the dislocations are also stable and a reversible strain amplitude is observed.

A plot of the critical surface stress to initiate plastic deformation versus the volume to surface area ratio (V/S) (*see supplementary figure 3*) is found to follow the generalized capillary equation,

$$\langle f \rangle = \frac{3}{2} \langle P \rangle \frac{V}{S},$$
 where a linear relationship is observed between these two quantities; the

slope of which is proportional to the mean pressure required to induce yielding, 3.6 GPa in this case. This value is on the order of the theoretical shear strength and also is in agreement with the results of MD simulations of gold nanowires[92].

When the potential Au4 is applied, a significant change in behavior is displayed. There is a rapid appearance of slip bands in the ligaments resulting in a fast densification of the structure. The massive dislocation pileup results in the formation of amorphous regions

in the structure. At room temperature, one may expect to form a nanocrystalline material rather than the amorphous structure observed in these simulations at 1 K.

Fig. 5 is a plot of the radial distribution function $g(r)$ for several timesteps during the relaxation with potential Au4. This shows the transition from a mostly crystalline material with relatively sharp peaks at the expected neighbor shell distances to a mostly amorphous material in which the peaks soften and broaden leaving in the end only one clearly distinguishable peak at the 1st neighbor shell distance.

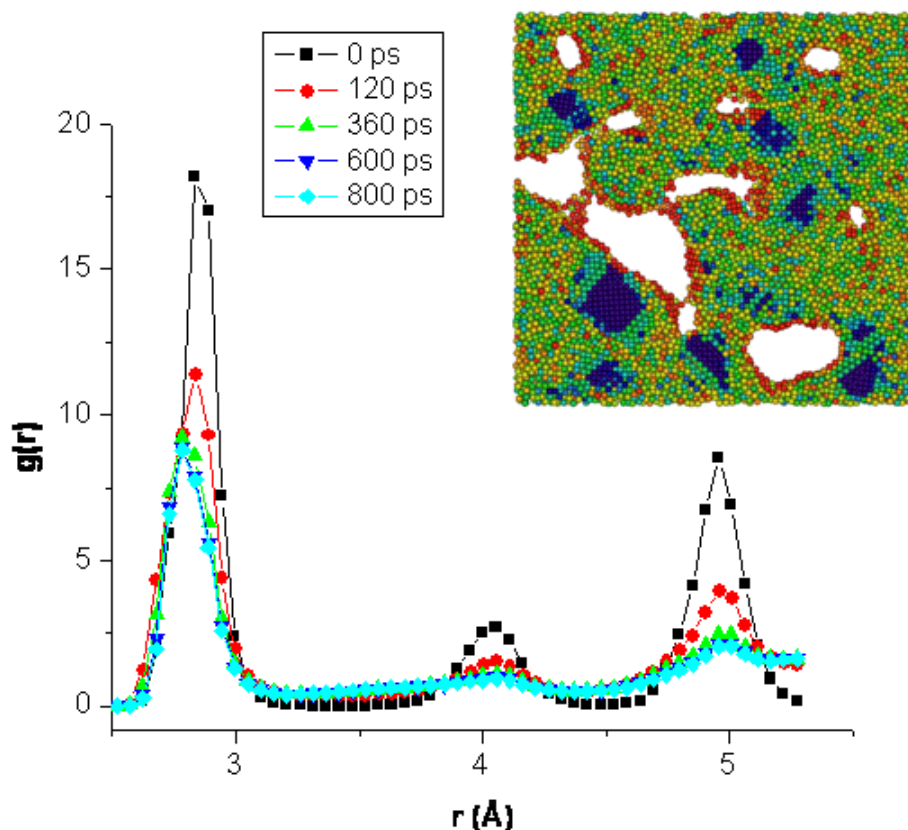


Figure 5-5 -- Mechanical instability of np-Au. Radial distribution function for several timesteps during the relaxation of the 1.8 nm diameter ligament sample with potential Au4 showing the transition to an amorphous structure. Inset shows the relaxed structure after 800 ps.

In conclusion, a phase-field model has been successfully utilized to generate model bicontinuous nanoporous gold structures amenable to atomistic simulations. Molecular dynamics simulations were then utilized to successfully determine the stability of these structures to surface stress. A critical mean pressure to induce yielding was found to be near the theoretical yield strength. There also exists a critical surface stress induced mean pressure above which the pore structures are unstable and a densification process proceeds.

5.1.3 Methods

Samples were prepared by cutting 0.7" x 0.7" square sheets from a 0.005" thick foil of $\text{Ag}_{0.7}\text{Au}_{0.3}$ which was previously annealed for 24 hours at 900 °C. The cut samples were then reannealed at 900 °C for 2 hours. Two samples were placed vertically in a quartz electrochemical cell in transmission geometry. Concentrated nitric acid was then circulated through the cell from a 500 ml reservoir to selectively remove the Ag from the alloy. SANS data was collected during the dealloying.

The SANS measurements were performed using an 8 meter long SANS instrument at the National Institute of Standards and Technology 20 MW reactor. The neutron beam was pinhole collimated. A beam wavelength of 5 Å was used for the early dealloying times (first 1 hour) and a wavelength of 15 Å was used for the latter period of the experiment (1 hour to 21 hours). The measurement range for the scattering vector, Q , was 0.012 to 0.21 Å⁻¹ for the 5 Å wavelength and 0.0038 to 0.072 Å⁻¹ for the 15 Å wavelength, where Q is defined as

$Q = \frac{4\pi}{\lambda} \sin(\theta/2)$ and θ is the scattering angle. The absolute scattering was determined

using a polystyrene-as2 standard for the 15 Å wavelength and a 1 mm water standard for the 5 Å wavelength.

5.1.4 Acknowledgements

S.G. Corcoran acknowledges support by the National Science Foundation under Grant No. DMR - 9975190 and DMR – 0301007. D. Farkas acknowledges support by the NSF – Materials Theory. This work utilized facilities supported in part by the National Science Foundation under Agreement No. DMR-9986442. We acknowledge the support of the National Institute of Standards and Technology, U.S. Department of Commerce, in providing the neutron research facilities used in this work. The authors would also like to acknowledge discussions with Karl Sieradzki and also Jonah Erlebacher.

5.1.5 Supplemental Material

i.) Comparison of chord lengths in experimental np-Au and Phase Field generated np-Au

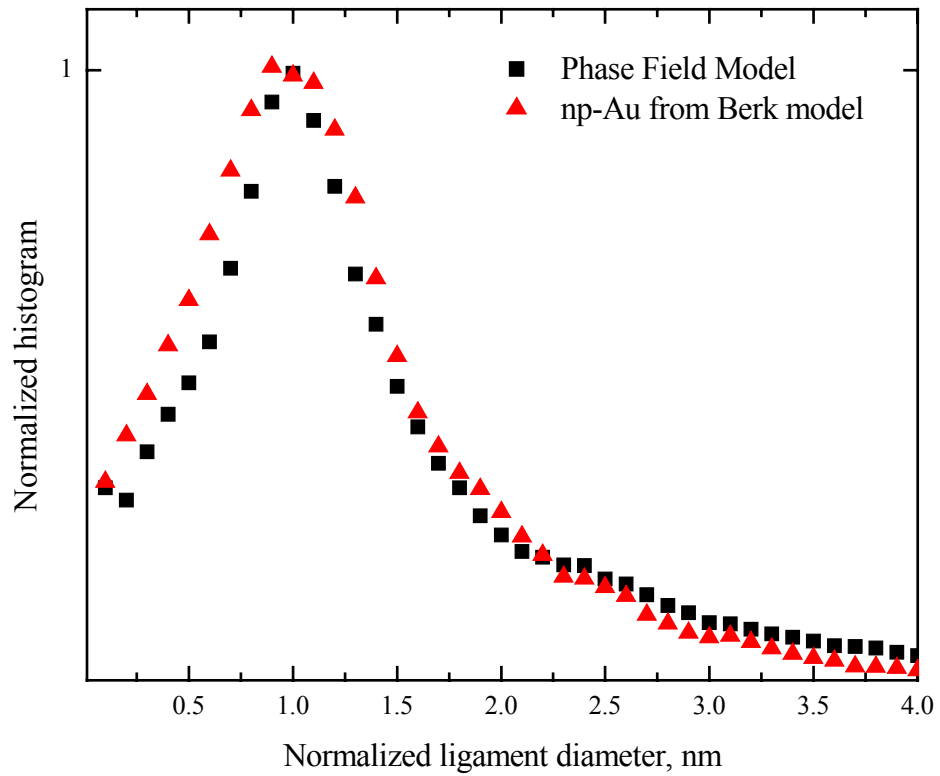


Figure 5-6 -- Length measurement comparison between the bicontinuous structures generated by the phase field model as compared to those generated by the Berk model based on the distribution in wavelengths measured by small angle neutron scattering for dealloyed np-Au.

(ii) Relaxed np-Au showing presence of plastic deformation

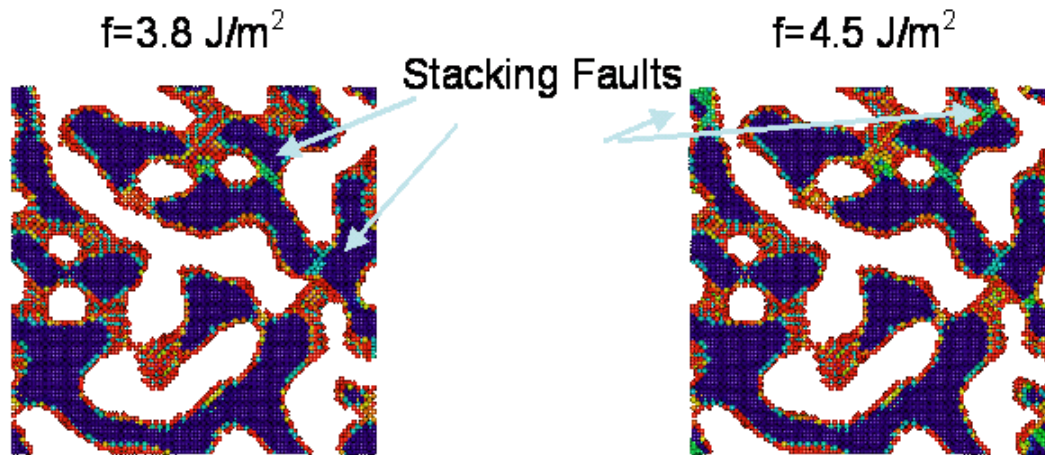


Figure 5-7 -- Plastic deformation induced by surface stress values of 3.8 and 4.5 J / m² as indicated. The presence of stacking faults is indicated in the figures.

(iii) Critical surface stress observed to cause plastic deformation

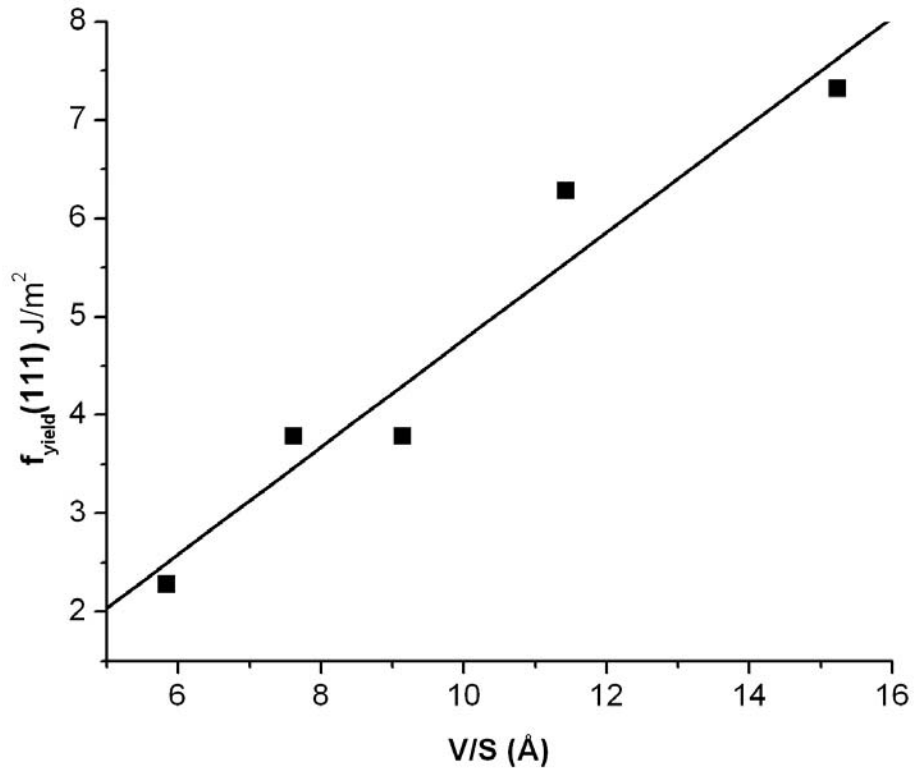


Figure 5-8 -- Critical surface stress to initiate plastic deformation versus the volume to surface area ratio. The points correspond to the samples with ligament diameters of 1.5, 1.8, 2.1, 2.7, and 3.6 nm. The samples with ligament diameters of 1.3 and 1.4 nm were unstable to all of the potentials of Table 5-1.

(iv) Simulated surface stress induced amorphization of nanoporous gold

When the potential Au2 is applied, a significant change in behavior is displayed. There is a rapid appearance of slip bands in the ligaments resulting in a fast densification of the structure. The massive dislocation pileup results in the formation of amorphous regions in the structure. These amorphous regions continue to grow with time and almost entirely consume the crystalline regions of the sample.

Figure 5-9 is a plot of the radial distribution function $g(r)$ for several timesteps during the relaxation with potential Au2. This shows the transition from a mostly crystalline material with relatively sharp peaks at the expected neighbor shell distances to a mostly amorphous material in which the peaks soften and broaden leaving in the end only one clearly distinguishable peak at the 1st neighbor shell distance. This amorphization is most likely due to the low temperature and high speed of the densification.

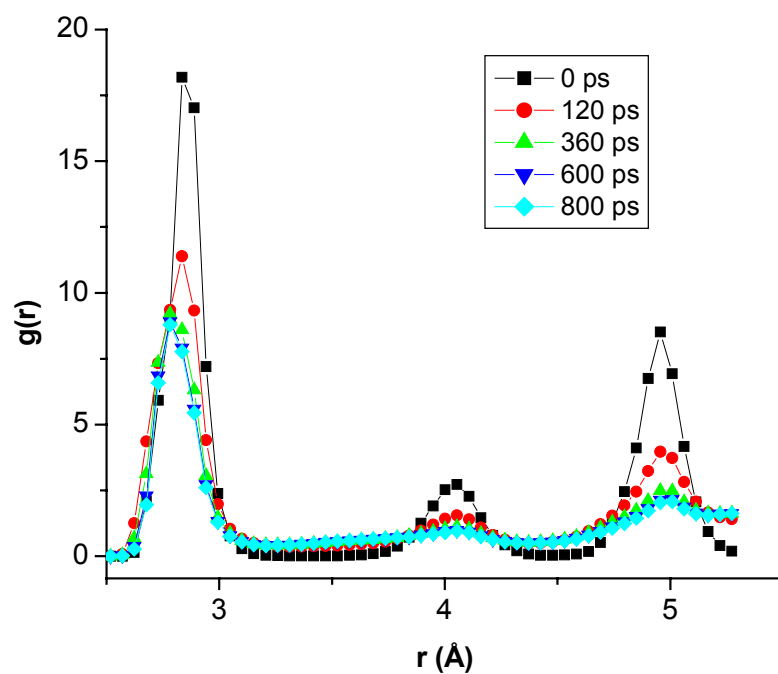


Figure 5-9 – Radial distribution function for several timesteps during the densification of the 1.8 nm ligament size sample subjected to a surface stress of 6.3 J/m^2 . The broadening and diminishing of the 2nd and 3rd neighbor shell peaks is indicative of amorphization.

CHAPTER 6 Conclusions

A method of digitally creating quantitatively representative nanoporous structures has allowed us the opportunity to use atomic scale simulations to explore the stability of macroscopic materials with a nanometer scale structure.

The geometric volume change of np-structures has been shown to be significantly dependent upon surface relaxation in addition to the curvature dependent mean pressure given by the generalized capillary equation. We have shown that this is a reasonable expectation for spherical particles and np-solids based on the magnitude of the surface relaxation term and agrees with the observed actuation measurements in the literature.

Molecular dynamics simulations were then utilized to successfully determine the stability of these structures to surface stress. A critical mean pressure to induce yielding was found to be near the theoretical yield strength. There also exists a critical surface stress induced mean pressure above which the pore structures are unstable and a densification process proceeds.

APPENDIX A

Reprinted with permission from Phys. Rev. Lett. 95, 075702 (2005) by A. Caro, D.A. Crowson and M. Caro. Copyright 2005 by the American Physical Society.

<http://link.aps.org/abstract/PRD/v95/e075702>

Classical Many-Body Potential for Concentrated Alloys and the Inversion of Order in Iron-Chromium Alloys

A. Caro, D.A. Crowson, and M. Caro

Atomistic simulations of alloys at the empirical level face the challenge of correctly modeling basic thermodynamic properties. In this Letter we propose a methodology to generalize many-body classic potentials to incorporate complex formation energy curves. Application to Fe-Cr allows us to correctly predict the order vs segregation tendency in this alloy, as observed experimentally and calculated with *ab initio* techniques, providing in this way a potential suitable for radiation damage studies.

Computational materials science is nowadays a standard approach to study complex problems in solids. Besides *ab initio* techniques, a great interest exists for classic approaches adequate for a large number of atoms, as needed in studies of large crystalline defects with long range interactions. The requirement of accurate, predictive simulation tools points towards the necessity of models for the interactions that are able to reproduce important fundamental properties of materials. Usually the models used are known as “many-body” potentials, grouped in large categories as the embedded-atom models and the second-moment approximation[93]. Most of the vast amount of work done using

these classic potentials addresses either pure elements or intermetallic compounds; only a few address concentrated alloys.

Based on the enormous success of these many-body potentials for large scale atomistic simulations of materials[94, 95], there has been a continuous progress in the field since its inception, extending the models towards increasingly complex materials like bcc, covalent, ordered compounds and dilute alloys. In this Letter, we focus on concentrated alloys with complex heat of formation, and provide a methodology to address arbitrarily complex systems. This methodology is applied to Fe-Cr, a system of interest in fission and fusion technology as structural material with good mechanical, thermal and radiation properties. Computer simulation studies of radiation damage in these alloys require models that can adequately predict alloy stability-microstructure evolution under large doses.

The so-called many-body potentials have in common a description of the total energy in terms of the sum over atom energies, themselves composed of two contributions, namely, embedding and pair potential terms. For heteroatomic systems, let us say binary alloys involving elements A and B, it reads

$$E = \sum_i^N \left[F_{\alpha_i} \left(\sum_{j \neq i} \rho_{\alpha_i \beta_j}(r_{ij}) \right) + \frac{1}{2} \sum_{j \neq i} V_{\alpha_i \beta_j}(r_{ij}) \right], \quad (1)$$

Where alpha and beta stand for elements A and B sitting at sites i and j , F 's are the embedding functions for either type of elements, and V 's and ρ 's are the pair potentials

and densities between alpha-beta pairs. Alloy properties are therefore described by the functions ρ_{AB} and V_{AB} . Depending on the model considered, the density functions do not always include the cross term ρ_{AB} . Different expressions for the embedding energies, densities, and pair potentials englobe a large diversity of similar models.

In recent papers we addressed the problem of alloy description with atomistic models from the perspective of thermodynamics rather than the properties of a single impurity. We developed numerical tools to calculate free energies of the relevant phases and applied them to a couple of systems, namely, Au-Ni[96] and Fe-Cu[97]. Both of these systems have in common the fact that the formation energy of the alloy is a rather symmetric function of the composition and, as it is shown below, a standard approach using a cross pair potential term was enough to reproduce their properties. We found that alloy models fitted to properties of the dilute limit usually show erroneous behavior in the concentrated case. For Fe-Cr, in particular, this problem is at the core of the limitations of the classic potentials due to the highly nonsymmetric formation energy that even changes sign at low Cr composition[49].

Focusing our attention on disordered alloys, the strategies to develop alloy potentials have been at least twofold: perform a global optimization of all functions in Equation (1) together to match the targeted properties of A, B, and AB systems, or start by developing potentials for pure A and pure B, and then fit the alloy properties by adjusting the cross terms in that equation. By far, most of the work done on alloys has used the dilute heat

of solution as the key alloy property to fit, but, in general, the description of concentrated alloys requires more information than that contained in this sole quantity.

A convenient way to analyze alloy properties with independence of the pure elements is to discuss excess quantities, i.e., quantities measured with respect to the ideal solution. Ideal solutions, by definition, have null excess quantities and their energy, Equation (1), is given by the linear interpolation between the two constituents. To construct models that depart from ideality, we can use either or both terms in Equation (1). It is important to notice that even without using a cross density, the embedding term always introduces a heat of formation, i.e., a nonlinearity of energy vs composition, through the nonlinear functions $F(p(x))$.

In this work, we follow the strategy of using potentials for the pure elements already available in the literature, thereby taking advantage of the continuous progress in the field. We then adjust the alloy terms, focusing on the nonlinearities built upon the pair potential cross term alone. To this end, we use a representation that minimizes the nonlinear contribution of the embedding term. We start with a preparation of the two pure element potentials in a way that is adequate for our purpose, that is, the effective representation with normalized densities, which for $\alpha=A, B$ reads

$$\begin{aligned}\rho_\alpha &= \rho_\alpha^o / \zeta_{\alpha,eq}^o \\ F_\alpha(\zeta_\alpha) &= F_\alpha^o(\zeta_\alpha^o) - F_\alpha^{o'}(\zeta_{\alpha,eq}^o) \zeta_\alpha^o \\ V_{\alpha,\alpha}(r) &= V_{\alpha,\alpha}^o(r) + 2F_\alpha^{o'}(\zeta_{eq}^o) \rho_\alpha^o(r)\end{aligned}\tag{2}$$

Where the superscript o stands for original, $\zeta_{\alpha,eq}^o$ for the density on a lattice site at equilibrium, $\left[\sum_{j \neq i} \rho_{\alpha_i} (r_{ij}^{eq}) \right]$, and the prime ' for derivative. These transformations do not alter the properties of the pure elements but have the advantage of minimizing the contribution of the embedding term to the formation energy of the alloy, as is discussed below, and allow us to combine potentials for pure elements coming from different authors with eventually very different and unrelated magnitudes of the densities. In this work, we use the Fe potential reported in [98] and the Cr potential reported in [99].

The free energy of a random solid solution phase of an alloy with composition x at temperature T is conveniently expressed as

$$g(x, T) = g_{ref}(x, T) + g_{mix}(x, T) + \Delta g(x, T), \quad (3)$$

where g_{ref} is the compositional weighted free energy of the pure components, give by
 And g_{mix} is the free energy contribution form the entropy of mixing for a random alloy,
 The excess Gibbs energy of mixing is conveniently expressed by a Redlich-Kister expansion as

$$\Delta g(x, T) = x(1-x) \sum_{p=0}^n L_p(T) (1-2x)^p, \quad (4)$$

Where L_p is the p th-order binary interaction parameter; in general, it is a function of temperature. Because of the complexity that represents fitting potentials to actual temperature dependent functions, in what follows we adopt two important simplifications: neglecting the excess vibrational entropy and assuming that the formation energy does not depend on T . This simplifies Equation (4) to

$$\Delta g(x, T) \cong \Delta H(x) = x(1-x) \sum_{p=0}^n L_p (1-2x)^p \quad (5)$$

For Fe-Cr the formation energy has recently been calculated ab initio [49] together with a rough estimate of the bulk modulus B and lattice parameter of the alloy a_0 . These calculations contain several simplifications, as Fe and Cr both have magnetism, and are therefore not to be considered as the definitive values classic models have to reproduce, but as first estimates upon which classic models can be developed. From those results, we consider the formation energy as our single target function to be reproduced.

From Figure (5) in Ref. [49] the formation energy of bcc ferromagnetic Fe-Cr alloys can be reproduced by a Redlich-Kister expansion, Equation (5), to 4th order in $(1-2x)$. Table I gives the corresponding coefficients in electron volts.

To find the functional form of the cross potential, we need an analytic model for the alloy. We adopt a model in which the species that sits on site I can be either A or B, but both are embedded in the same average environment, as discussed by Ackland and Vitek [94]:

$$E^{rand} = x_A^2 \sum V_{AA}(r_{ij}) + x_B^2 \sum V_{BB}(r_{ij}) + 2x_A x_B \sum V_{AB}(r_{ij}) + x_A F_A(\tilde{\rho}) + x_B F_B(\tilde{\rho}) \quad (6)$$

with $\tilde{\rho} = x_A \sum \rho_A(r_{ij}) + x_B \sum \rho_B(r_{ij})$

The contribution of the embedding terms to the energy of mixing, is

$$\Delta E^{emb} = x_A [F_A(\tilde{\rho}) - F_A(\tilde{\rho}=1)] + x_B [F_B(\tilde{\rho}) - F_B(\tilde{\rho}=1)] \quad (7)$$

By making a Taylor development of F around $\tilde{\rho} = 1$ and using Equation (2), we see that this contribution is quadratic in $(\tilde{\rho} - 1)$ and therefore small for small variations in $\tilde{\rho} - 1$:

$$\Delta E^{emb} = x_A F_A''(\tilde{\rho}=1)(\tilde{\rho}-1)^2 + x_B F_B''(\tilde{\rho}=1)(\tilde{\rho}-1)^2 \quad (8)$$

For the potentials we use in this work, the transformations (2), in fact, drop the contribution to the embedding term to the formation energy down to ~ 1 meV/atom at $x=0.5$, making it negligible when compared to the target for this alloy ~ 100 meV/atom [49]. This in practice leaves the pair potential as the sole contributor to the formation energy. The contribution to the energy of mixing from the pair potential terms is

[replacing for short $\sum V_{AA}(r_{ij})$ by v_A , and so on and $x_B = x$, $x_A = 1-x$],

$$\Delta E^{pair} = x(1-x) \{2v_{AB} - (v_A + v_B)\} \quad (9)$$

We now introduce our proposition for the alloy potential based on the following points:

(i) Taking advantage of the result Equation (8), we build up the nonlinearity upon the pair potential alone (this is a simplification adopted for this case in particular; it can easily be removed in other cases where TO uses either or both contributions). (ii) We assume that V_{AB} is a function of both (x,r) , that can be separated into a product $h(x)u_{AB}(r)$ and we then choose

$$V_{AB}(x,r) = h(x) \frac{1}{2} [V_{AA}(r) + V_{BB}(r)] \quad (10)$$

This election of the cross pair potential allows us to describe any type of formation energy curves, giving an ideal solution for $h(x) = 1$, a regular solution with positive or negative heat of mixing for $h(x) \neq 1$, and an arbitrary complex heat of mixing for $h(x)$, a polynomial on x . We also see that without introducing a polynomial on x we cannot go beyond symmetric formation energies [i.e., only L_0 in the expansion Equation (4)].

Equation (10) also shows that if the target function is a fourth order Redlich-Kister polynomial, so will $h(x)$ be. It then provides us with a hint as to what functional form to use in the optimization procedure.

We replace now $V_{AB}(r_{ij})$ in Equation (6) by $h(x) \frac{1}{2} [V_{AA}(r_{ij}) + V_{BB}(r_{ij})]$ and, by minimizing the difference between this expression for the energy and the target formation

energy [Equation (5) and Table I], at the lattice parameter that minimizes the energy, we find the coefficients of $h(x)$, reported in Table II.

Table A-1. Values of the Redlich-Kister expansion coefficients, Equation (5), corresponding to

ΔH_{Fe-Cr}^{mix} **from Rf. [6], in eV.**

L_0	L_1	L_2	L_3	L_4
0.41566	0.0814134	-0.0101899	0.267659	-0.248269

Table A-2. Coefficients of the 4th order polynomial $h(x)$ in Equation (10, with values extracted from a global minimization as explained in the text.

h_0	h_1	h_2	h_3	h_4
0.883644	-0.059302	0.644634	-1.342524	0.918932

It is interesting to point out that if Equation (8) gives a really small contribution, as is the case for these two pure element potentials in the effective representation, we can neglect altogether the contribution of the embedding terms. Then, by equating Eqs. (5) and (9) instead of minimizing a target function, we can define $h(x)$, the composition dependence of the cross potential, through an identity, namely,

$$[h(x)-1](v_A + v_B) \approx \sum_{p=0}^n L_p (1-2x)^p \quad (11)$$

The formation energy, the lattice parameter, and the bulk modulus of the resulting alloy are shown in Figure A-1. The bulk modulus shows a small softening with respect to linearity of about 5 GPa at $x \approx 0.5$ that in terms of the absolute value of B represents a change of 3%. The lattice parameter is linear with 0.1%. The formation energy in turn shows a curve indistinguishable from the target function extracted from Ref. [49]. In summary, the potential reproduces extremely well the energy, lattice parameter, and bulk modulus.

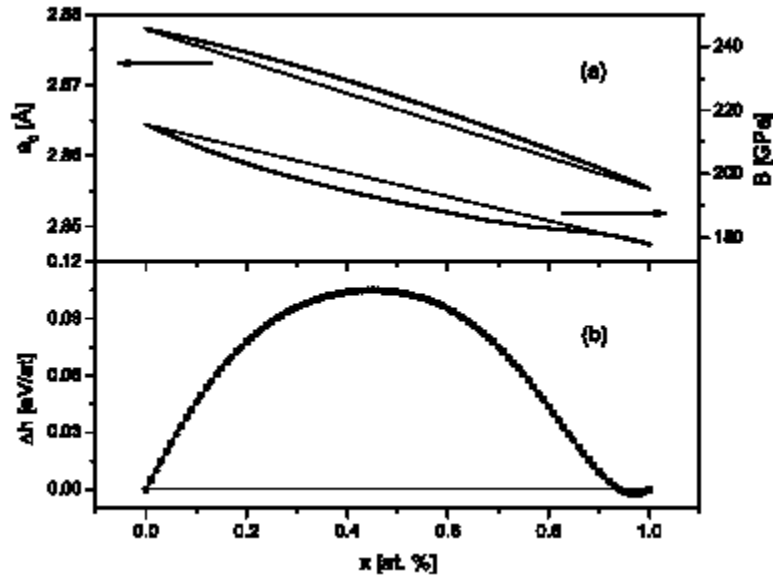


Figure A-1-- Variations of bulk modulus B and lattice parameter a_0 (a), and formation energy of the alloy (b) as a function of Fe composition. Thin straight lines represent the linear interpolation corresponding to the ideal solution. Maximum departures for B and a_0 from ideal behavior are 2.5% and 0.1%, respectively.

Figure A-2 shows that the polynomial $h(x)$ that results from the fitting procedure is a smooth function of x , close to $h = 1$, and that it crosses the line $h = 1$ at $x = 0.94$, the composition at which the alloy behaves as ideal, as expected.

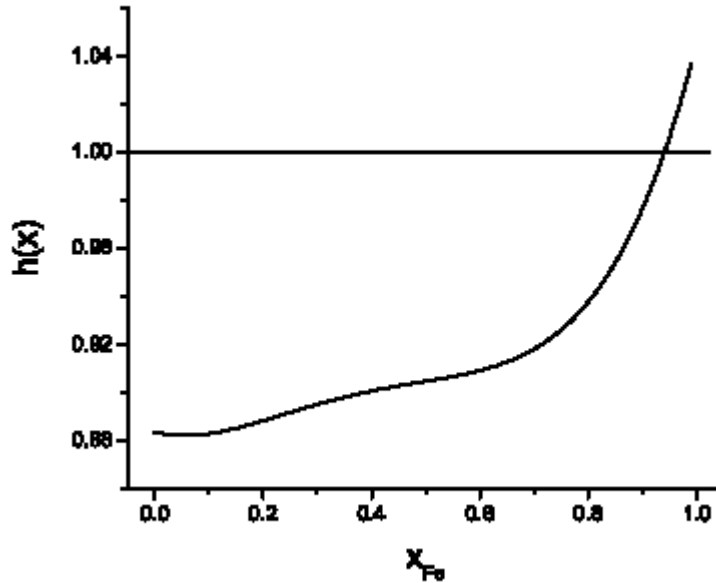


Figure A-2. Polynomial $h(x)$ representing the composition dependence of the cross potential versus Fe composition, according to Equation (11).

The final requirement for practical applications is to define the composition x to be used in a simulation that for heterogeneous materials becomes a function of position. A sound choice is to use the partial B density (i.e., the component of the total density at atoms I and j originated by B atoms at neighboring sites l). The density on a lattice site i , ζ_i , is

given by $\sum_l \rho_{\beta l}(r_{il})$, where the sum runs over the neighbors of i , and β stands for elements A or B sitting on the site l . The sum can be decomposed into partial contributions $\zeta_i = \sum_l' \rho_A(r_{il}) + \sum_l' \rho_B(r_{il}) = \zeta_i^A + \zeta_i^B$, where the ' in the sum means neighbors of i occupied by atoms of type A, and similarly " means B occupancy. In this way, the composition to be used in a pair term involving sites i and j can conveniently be defined as

$$x_{i,j} = \frac{1}{2}(x_i + x_j) = \frac{1}{2} \left(\frac{\zeta_i^B}{\zeta_i} + \frac{\zeta_j^B}{\zeta_j} \right) \quad (12)$$

This definition provides a well behaved function, adequate for force calculations.

To test the new potential and its ability to reproduce the ordering tendencies measured experimentally, we have run Metropolis Monte Carlo simulations in the transmutation ensemble with displacements at 500 K and determined the Warren-Cowley [100] short range order parameter of the first neighbor shell. We used 500 K because the order is so weak that at 700 K it is comparable to the noise. Results are reported in Figure 3, together with the experimental results from Ref. [101] at 700 K.

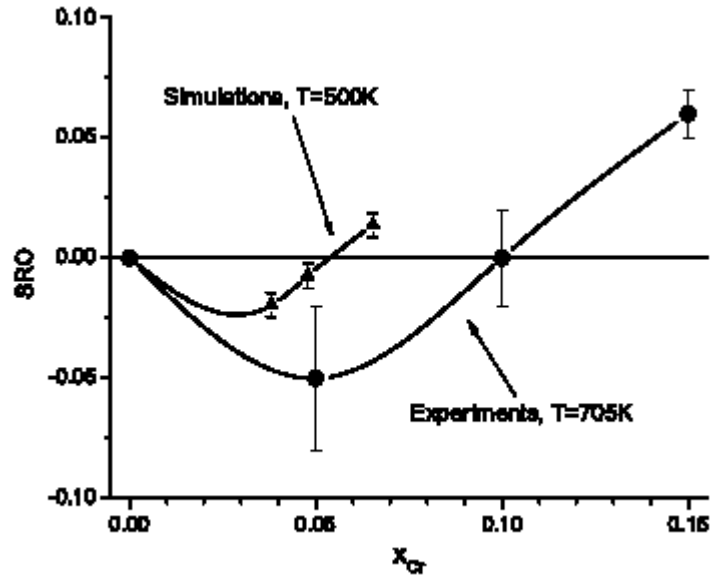


Figure A-3. Short range order parameter versus Cr composition as calculated by Monte Carlo simulations with the new potential and experimental measurements from [11].

Inversion of order in Fe-Cr has been predicted long ago, with a change in sign at $x=0.25$ [102]. First measurements found it at $x = 0.10$ [101]. With the *ab initio* data we used to develop the potential, with the maximum strength of the negative formation energy being only a few meV/atom, the maximum order obtained at 500 K is only -0.025, while the experimental result at even higher temperature is close to its maximum possible value $-x/(1-x) \approx -0.05$. This discrepancy raises doubts about the accuracy of the *ab initio* prediction.

In conclusion, we present a general procedure to derive a potential for a complex alloy and apply it to the case of Fe-Cr using the heat of solution as reported by [49]. Even if the target function is probably not the definitive *ab initio* result for this alloy, the

procedure proposed in this Letter can be used to reproduce any function of the composition.

Discussions with P. Turchi and L. Malerba are gratefully acknowledged. This work was performed under the auspices of the U.S. Department of Energy of the University of California Lawrence Livermore National Laboratory under Contract No. W-7405-ENG-48. D.A. Crowson acknowledges support for this work by the National Science Foundation under Grant No. DMR-0301007.

BIBLIOGRAPHY

1. Lechtman, H., *Pre-Columbian Surface Metallurgy*. Scientific American, 1984. **250**: p. 56.
2. <http://www.corrosion-doctors.org/Forms/dealloy.htm>.
3. K. Sieradzki, J.S.K., A.T. Cole, R.C. Newman, *The Relationship Between Dealloying and Transgranular Stress Corrosion Cracking of Cu-Zn and Cu-Al Alloys*. J. Electrochem. Soc., 1987. **134**: p. 1635.
4. R.G. Kelly, A.J.F., T. Shahrabi, and R.C. Newman, *Brittle Fracture of an Au/Ag Alloy Induced by a Surface Film*. Met. Trans. A, 1991. **22A**: p. 531.
5. T.B. Cassagne, W.F.F., and B.D. Lichter, *On the Failure Mechanism of Chemically Embrittled Cu₃Au Single Crystals*. Met. Trans. A, 1986. **17A**: p. 703.
6. J.S. Chen, T.M.D., and M. Salmeron, *Brittle Fracture of Cu-30Au Induced by a Surface Layer*. J. Electrochem. Soc., 1992. **139**: p. L55.
7. R.C. Newman, R.R.C., and K. Sieradzki, *Evidence for Dealloying of Austenitic Stainless Steels in Simulated Stress Corrosion Crack Environments*. Br. Corros. J., 1989. **24**: p. 143.
8. A. Dursun, D.V.P., S.G. Corcoran, *Dealloying of Ag-Au Alloys in Halide Containing Electrolytes: Affect on Critical Potential and Pore Size*. Journal of the Electrochemical Society, 2003. **150**(7): p. B355-B360.
9. Corcoran, S.G., *The Morphology of Alloy Corrosion*. Proc. of the Electrochem. Soc., Symp. on Critical Factors in Localized Corrosion III, 1999: p. 500-507.
10. Erlebacher, J., et al., *Evolution of nanoporosity in dealloying*. Nature, 2001. **410**(6827): p. 450.

11. Hieda, M., et al., *Ultrasensitive quartz crystal microbalance with porous gold electrodes*. Applied Physics Letters, 2004. **84**(4): p. 628-630.
12. Baughman, R.H., *Muscles Made from Metal*. Science, 2003. **300**: p. 268-269.
13. Weissmuller, J., et al., *Charge-Induced Reversible Strain in a Metal*. Science, 2003. **300**: p. 312-315.
14. Dominik Kramer, R.N.V., Jorg Weissmuller, *Surface-Stress Induced Macroscopic Bending of Nanoporous Gold Cantilevers*. Nano Letters, 2004. **4**(5): p. 793-796.
15. Li, R. and K. Sieradzki, *Ductile-Brittle Transition in Random Porous Au*. Physical Review Letters, 1992. **68**(8): p. 1168-1171.
16. Corcoran, S.G., *Dealloying*, in *ASM Handbook*. 2003.
17. Calvert, C. and R. Johnson, *Actions of Acids upon Metals and Alloys*. Journal of the Chemical Society, 1866. **19**: p. 434-454.
18. Moore, H., S. Bechinsale, and C.E. Mallinson, *The Season-Cracking of Brass and Other Copper Alloys*. Journal of the Institute of Metals, 1921. **25**: p. 35-153.
19. Abrams, R.B., *The Dezincification of Brass*. Transactions of the American Electrochemical Society, 1922. **XLII**: p. 39-54.
20. Pickering, H.W. and C. Wagner, Journal of the Electrochemical Society, 1967. **114**(7): p. 698-706.
21. Pickering, H.W., *Characteristic Features of Alloy Polarization Curves*. Corrosion Science, 1983. **23**: p. 1107.
22. Forty, A.J., *Fundamental Aspects of Stress Corrosion Cracking*. 1967: p. 64-71.
23. Sieradzki, K. and R.C. Newman, *Stress-corrosion cracking*. Journal of Physics and Chemistry of Solids, 1987. **48**(11): p. 1101-1113.

24. Sieradzki, K., et al., *Computer-Simulations of Corrosion -- Selective Dissolution of Binary--Alloys*. Philosophical Magazine A, 1989. **59**(4): p. 713-746.
25. Sieradzki, K., *Curvature Effects in Alloy Dissolution*. Journal of the Electrochemical Society, 1993. **140**(10): p. 2868-2872.
26. Dursun, A., *Ph.D. Thesis, Virginia Polytechnic Institute and State University*. 2003.
27. Dursun, A., D.V. Pugh, and S.G. Corcoran, *Dealloying of Ag-Au Alloys in Halide Containing Electrolytes: Affect on Critical Potential and Pore Size*. Journal of the Electrochemical Society, 2003. **150**(7): p. B355-B360.
28. Gleiter, H., et al., *Nanocrystalline Materials: A Way to Solids with Tunable Electronic Structures and Properties*. Acta Materialia, 2001. **49**: p. 737-745.
29. Shuttleworth, R., *The Surface Tension of Solids*. Proc. R. Soc. London Ser.A, 1950. **63**: p. 444.
30. Lin, K.F. and T.R. Beck, *Surface Stress Curves for Gold*. Journal of the Electrochemical Society, 1976. **123**: p. 1145-1151.
31. Friesen, C., et al., *Surface Stress and Electrocapillarity of Solid Electrodes*. Langmuir, 2001. **17**: p. 807-815.
32. Weissmuller, J. and J.W. Cahn, *Mean stresses in microstructures due to interface stresses: A generalization of a capillary equation for solids*. Acta Materialia, 1997. **45**(5): p. 1899-1906.
33. Srolovitz, P.D.B.a.D.J., *Elastic fracture in random materials*. Physical Review B, 1988. **37**(10): p. 5500-5507.
34. P.M. Duxbury, P.L.L., and P.D. Beale, *Breakdown properties of quenched random systems: The random-fuse network*. Physical Review B, 1987. **36**(1): p. 367-380.

35. B. Kahng, G.G.B., S. Redner, L. de Arcangelis and H.J. Herrmann, *Electrical breakdown in a fuse network with random, continuously distributed breaking strengths*. Physical Review B, 1988. **37**(13): p. 7625-7637.
36. C. Moukarzel, a.P.M.D., *Failure of three-dimensional random composites*. J. Appl. Phys., 1994. **76**(7): p. 4086-4094.
37. Rong Li, K.S., *Ductile-Brittle Transition in Random Porous Au*. Physical Review Letters, 1992. **68**(8): p. 1168-1171.
38. F. Friedersdorf, K.S., *Film-Induced Brittle Intergranular Cracking of Silver-Gold Alloys*. Corrosion, 1996. **52**(5): p. 331-336.
39. Shanno, D.F. and K.H. Phua, *ACM Transactions on Mathematical Software* 6, 1980: p. 618-622.
40. Laplace, P.S.m.d., *A philosophical essay on probabilities*. 1951.
41. Haile, J.M., *Molecular Dynamics Simulation*. 1992.
42. Murray S. Daw, M.I.B., *Semiempirical, Quantum Mechanical Calculation of Hydrogen Embrittlement in Metals*. Physical Review Letters, 1983. **50**(17): p. 1285-1288.
43. Johnson, R.A., *Analytic nearest-neighbor model for fcc metals*. Physical Review B, 1988. **37**(8): p. 3924-3931.
44. Trimble, T.M., R.C. Cammarata, and K. Sieradzki, *The stability of fcc (111) metal surfaces*. Surface Science, 2003. **531**: p. 8-20.
45. M. Haftel, a.M.R., *Surface embedded atom model of the electrolyte-metal interface*. Physical Review B, 2001. **64**: p. 195405.
46. F. Ercolessi, E.T., and M.Parrinello, *Au (100) Surface Reconstruction*. Physical Review Letters, 1986. **57**(6): p. 719-722.
47. Turchi, P.E.A. and A. Gonis, *First-principles study of stability and local order in substitutional Ta-W alloys*. Physical Review B, 2001. **64**: p. 085118-8.

48. M.W. Finnis, J.E.S., *A simple empirical N-body potential for transition-metals*. Philosophical Magazine A, 1984. **50**(1): p. 45-55.
49. Olsson, P., et al., *Ab initio formation energies of Fe-Cr alloys*. Journal of Nuclear Materials, 2003. **321**: p. 84-90.
50. Caro, A., D.A. Crowson, and Magdalena, *Classical Many-Body Potential for Concentrated Alloys and the Inversion of Order in Iron-Chromium Alloys*. Physical Review Letters, 2005. **95**: p. 075702.
51. Corcoran, S.G., *Effects of Metallurgical Variables on Dealloying Corrosion*, in *ASM Handbook, Corrosion: Fundamentals, Testing, and Protection*, S.D. Cramer and B.S. Covino Jr., Editors. 2003, ASM International: Materials Park, OH. p. 287-293.
52. Sieradzki, K., et al., *The Relationship Between Dealloying and Transgranular Stress-Corrosion Cracking of Cu-Zn and Cu-Al Alloys*. Journal of the Electrochemical Society, 1987. **134**(7): p. 1635-1639.
53. Kelly, R.G., et al., *Brittle Fracture of an Au/Ag Alloy Induced by a Surface Film*. Metallurgical Transactions A, 1991. **22A**: p. 531-541.
54. Cassagne, T.B., W.F. Flanagan, and B.D. Lichter, *On the Failure Mechanism of Chemically Embrittled Cu₃Au Single Crystals*. Metallurgical Transactions A, 1986. **17A**: p. 703-710.
55. Chen, J.S., T.M. Devine, and M. Salmeron, *Brittle Fracture of Cu-30Au Induced by a Surface Layer*. Journal of the Electrochemical Society, 1992. **139**(6): p. L55-L57.
56. Newman, R.C., R.R. Corderman, and K. Sieradzki, *Evidence for Dealloying of Austenitic Stainless Steels in Simulated Stress Corrosion Crack Environments*. British Corrosion Journal, 1989. **24**(2): p. 143-148.
57. Li, R. and K. Sieradzki, *Ductile - Brittle Transition in Random Porous Au*. Physical Review Letters, 1992. **68**(8): p. 1168-1171.

58. Dursun, A., D.V. Pugh, and S.G. Corcoran, *Dealloying of Ag-Au Alloys in Halide Containing Electrolytes: Affect on Critical Potential and Pore Size*. Journal of the Electrochemical Society, 2003. **150**(7): p. B355-B360.
59. Ding, Y., M. Chen, and J. Erlebacher, *Metallic Mesoporous Nanocomposites for Electrocatalysis*. Journal of the American Chemical Society, 2004. **126**(22): p. 6876-6877.
60. Ertenberg R.W., A.B., Takano Y., *Prospects of porous gold as a low-temperature heat exchanger for liquid and solid helium*. Physica B, 2000. **284**: p. 2022-2023.
61. Yoon, J. and M.H.W. Chan, *Superfluid Transition of ^4He in Porous Gold*. Physical Review Letters, 1997. **78**(25): p. 4801-4804.
62. Lin, K.F. and T.R. Beck, *Surface stress curves for gold*. JECS, 1976. **123**(8): p. 1145.
63. Weissmuller, J. and D. Kramer, *Balance of Force at Curved Solid Metal-Liquid Electrolyte Interfaces*. Langmuir, 2005. **21**: p. 4592-4603.
64. Weissmuller, J. and J.W. Cahn, *Mean Stresses in Microstructures due to Interface Stresses: A Generalization of a Capillary Equation for Solids*. Acta Mater, 1997. **42**(5): p. 1899-1906.
65. Murray S. Daw, S.M.F., M.I. Baskes, *The embedded-atom method: a review of theory and applications*. Materials Science Reports, 1993. **9**: p. 251-310.
66. Robert C. Cammarata, K.S., *Surface and Interface Stresses*. Annu. Rev. Mater. Sci., 1994. **24**: p. 215-234.
67. Mays, C.W., J.S. Vermaak, and D.Kuhlmann-Wilsdorf, *On Surface Stress and Surface Tension II. Determination of the surface stress of gold*. Surface Science, 1968. **12**: p. 134-140.
68. Swaminarayan, S., R. Najafabadi, and D.J. Srolovitz, *Polycrystalline surface properties from spherical crystallites: Ag, Au, Cu and Pt*. Surface Science, 1994. **306**: p. 367-380.

69. Foiles, S.M., M.I. Baskes, and M.S. Daw, *Embedded-Atom-Method Functions for the FCC Metals Cu, Ag, Au, Ni, Pd, Pt, and their Alloys*. Physical Review B, 1986. **33**(12): p. 7983-7991.
70. Mays, C.W., J.S. Vermaak, and D. Kuhlmann-Wilsdorf, *On Surface Stress and Surface Tension II. Determination of the Surface Stress of Gold*. Surface Science, 1968. **12**: p. 134-140.
71. Jona, F. and P.M. Marcus, *The Structure of Surfaces II*. 1987. 90.
72. Newman, R.C., et al., *Alloy Corrosion*. MRS Bulletin, 1999. **24**(7): p. 24.
73. Chen, L.Q. and J. Shen, *Applications of semi-implicit Fourier-spectral method to phase field equations*. Computer Physics Communications, 1998. **108**: p. 147-158.
74. Hilliard, J.W.C.a.J.E., *Free energy of a nonuniform system. I. Interfacial Free Energy*. Journal of Chemical Physics, 1958. **28**(2): p. 258-267.
75. Berk, N.F., *Scattering Properties of the Leveled-Wave Model of Random Morphologies*. Physical Review A, 1991. **44**(8): p. 5069-5079.
76. Corcoran, unpublished data
77. Cahn, J.W., *Phase Separation by Spinodal Decomposition in Isotropic Systems*. The Journal of Chemical Physics, 1965. **42**: p. 93-99.
78. Berk, N.F., *Scattering Properties of the Leveled-Wave Model of Random Morphologies*. PRA, 1991. **44**(8): p. 5069-5079.
79. Sieradzki, K. and R.C. Newman, *Brittle Behavior of ductile Metals during Stress-Corrosion Cracking*. Philosophical Magazine A, 1985. **51**: p. 95-132.
80. Oppenheim, I.C., et al., *In situ Scanning Tunneling Microscopy of Corrosion of Silver-Gold Alloys*. Science, 1991. **254**: p. 687-689.
81. Ding, Y., Y.-J. Kim, and J. Erlebacher, *Nanoporous Gold Leaf: "Ancient Technology"/Advanced Material*. Advanced Materials, 2004. **16**(21): p. 1897-1900.

82. Sieradzki, K. and e. al, *The Dealloying Critical Potential*. Journal of the Electrochemical Society, 2002. **149**: p. B370-B377.
83. Forty, A.J. and P. Durkin, *A Micromorphological Study of the Dissolution of Silver-Gold Alloys in Nitric Acid*. Philosophical Magazine A, 1980. **42**: p. 295.
84. Ding, Y., M. Chen, and J. Erlebacher, *Metallic Mesoporous Nanocomposites for Electrocatalysis*. Journal of the American Chemical Society, 2004. **126**: p. 6876-6877.
85. Lavrik, N.V., et al., *Gold nanostructures for Transduction of Biomolecular Interactions into Micrometer Scale Movements*. Biomedical Microdevices, 2001. **3**: p. 35-44.
86. Kramer, D., R.N. Viswanath, and J. Weissmuller, *Surface-Stress Induced Macroscopic Bending of Nanoporous Gold Cantilevers*. Nano Letters, 2004. **4**(5): p. 793-796.
87. Berk, N.F., *Scattering Properties of a Model Bicontinuous Structure with a Well Defined Length Scale*. PRL, 1987. **58**(25): p. 2718-2721.
88. Teubner, M. and R. Strey, *Origin of the Scattering Peak in Microemulsions*. J. Chem. Phys., 1987. **87**(5): p. 3195-3200.
89. Cahn, J.W., *Phase Separation by Spinodal Decomposition in Isotropic Systems*. The Journal of Chemical Physics, 1965. **42**(1): p. 93-99.
90. Haftel, M. and M. Rosen, *Surface Embedded Atom Model of the Electrolyte-Metal Interface*. Physical Review B (Condensed Matter), 2001. **64**(19): p. 195405/1-196405/7.
91. Kelchner, C.L., S.J. Plimpton, and J.C. Hamilton, *Dislocation nucleation and defect structure during surface indentation*. Physical Review B, 1998. **58**(17): p. 11085-11088.
92. Hyde, B., H.D. Espinosa, and D. Farkas, *An Atomistic Investigation of Elastic and Plastic Properties of Au Nanowires*. JOM, 2005. **57**(9): p. 62-66.

93. Daw, M.S., S.M. Foiles, and M.I. Baskes, *The embedded-atom method: a review of theory and applications*. Materials Science Reports, 1993. **9**: p. 251-310.
94. Ackland, G.J. and V. Vitek, *Many-body potentials and atomic-scale relaxations in noble-metal alloys*. Physical Review B, 1990. **41**: p. 10324-10333.
95. Baskes, M.I., *Modified Embedded-Atom Potentials for Cubic Materials and Impurities*. Physical Review B, 1992. **46**(5): p. 2727-2742.
96. Arregui, E.O., M. Caro, and A. Caro, *Numerical evaluation of the exact phase diagram of an empirical Hamiltonian: Embedded atom model for the Au-Ni system*. Physical Review B, 2002. **66**(5): p. 054201.
97. Caro, A., et al., *Thermodynamics of an empirical potential description of Fe-Cu alloys*. Journal of Nuclear Materials, 2005. **336**(2-3): p. 233-242.
98. Mendeleev, M.I., et al., *Development of new interatomic potentials appropriate for crystalline and liquid iron*. Philosophical Magazine, 2003. **83**(35): p. 3977-3994.
99. Wallenius, J., et al., *Modeling of chromium precipitation in Fe-Cr alloys*. Physical Review B, 2004. **69**: p. 0941031-8.
100. Saunders, N. and A.P. Miodownik, *CALPHAD: A Comprehensive Guide*. 1998.
101. Mirebeau, I., M.Hennion, and G. Parette, *First Measurement of Short-Range-Order Inversion as a Function of Concentration in a Transition Alloy*. Physical Review Letters, 1984. **53**(7): p. 687-690.
102. Hennion, M., *Chemical SRO Effects in Ferromagnetic Fe Alloys in Relation to Electronic Band-Structure*. Journal of Physics F-Metal Physics, 1983. **13**: p. 2351.

Vita

Douglas A. Crowson

The author was born in Eau Claire, Wisconsin. He received his B.S. in Materials Science and Engineering from the University of Minnesota. Nearing completion of his undergraduate career he found employment with Hysitron Inc. in Minneapolis, MN. In 2000 he began his graduate studies at Virginia Tech under the advisement of Sean Corcoran and Diana Farkas. In the summers of 2004 and 2005 he worked at Lawrence Livermore National Laboratory as a technical scholar developing classical embedded atom method potentials for alloys with Alfredo Caro. He has now accepted a position in the scientific instrumentation industry.